

Multi-year analysis of rain-snow levels at Marquette, Michigan

J. A. Shates ¹, C. Pettersen ², T. S. L'Ecuyer ¹, M. S. Kulie ³

¹Department of Atmospheric and Oceanic Sciences, University of Wisconsin-Madison, Madison, Wisconsin

²Department of Climate and Space Sciences and Engineering, University of Michigan, Ann Arbor, MI

³Advanced Satellite Products Branch, NOAA/NESDIS/Center for Satellite Applications and Research,
Madison, Wisconsin

Key Points:

- Rain-snow levels are shallow in winter. In autumn and spring, rain-snow levels span the full range of the profiling radar.
- Rainfall microphysical characteristics and rates vary with rain-snow levels.
- Rain-snow levels determined from vertically profiling radar Doppler velocity correlate well with reanalysis derived melt levels.

Corresponding author: Julia Shates, shates@wisc.edu

This is the author manuscript accepted for publication and has undergone full peer review but has not been through the copyediting, typesetting, pagination and proofreading process, which may lead to differences between this version and the [Version of Record](#). Please cite this article as [doi: 10.1029/2022JD037132](https://doi.org/10.1029/2022JD037132).

This article is protected by copyright. All rights reserved.

Abstract

This study uses observations from a ground-based instrument suite to investigate the rain-snow level in stratiform rainfall from January 2014 to April 2020 in the Upper Great Lakes Region. The height above the surface where ice melts to rain, the rain-snow level (RSL), influences microphysical assumptions in remote sensing precipitation retrievals and the ability of space-based radar to discriminate surface precipitation phase because of ground clutter. The instrument suite is installed at the Marquette, MI (MQT) National Weather Service station adjacent to Lake Superior. Rain events and the RSL are studied through a ground-based vertically profiling radar (Micro Rain Radar), a custom NASA-developed video disdrometer (Precipitation Imaging Package), and reanalyses products from ECMWF ERA5 and NASA MERRA-2. Distinct macro and micro physical characteristics are observed in precipitation events with shallow RSL (< 1.8 km above ground level [AGL]) and intermediate RSL (> 1.8 km AGL). Intermediate RSL correspond to rain events with relatively higher rain rates and a higher concentration of small drops in the drop size distributions (DSDs). Shallow RSL DSDs contain relatively higher concentrations of large drops with lower fall speeds suggesting that partially melted snowflakes may be reaching the surface. Reflectivity-rain-rate relationships are also impacted by microphysical differences associated with RSL regimes. Radar-detected RSL agree with reanalysis-derived melt levels- especially at wet-bulb isotherms of 0.5°C and 1°C . Seasonal differences such as shallow rain-snow levels in winter, fall, and spring have subsequent implications for satellite detectability.

Plain Language Summary

The height above the surface where falling snow melts to rain, the rain-snow level, can be detected by both ground-based and space-based radars. However, space-based radars are limited in their ability to capture precipitation near the surface due to interference. This work investigates rain-snow levels between January 2014 and April 2020 from ground-based observations at the Marquette, MI National Weather Service office. This work includes observations from ground-based profiling radar and a custom NASA-developed instrument that records high resolution videos of precipitation at the surface. In addition, profile temperature and moisture data are used. These products are commonly used with satellite observations to determine the surface precipitation phase. The results show different characteristics for rain events with shallow and intermediate rain-snow levels. The radar-detected rain-snow levels illustrate good agreement with melt levels derived from reanalysis profile data, which is useful for satellite retrievals of precipitation. Seasonal differences such as shallow rain-snow levels in winter, fall, and spring have subsequent implications for satellite detectability.

1 Introduction

Precipitation is changing as the climate warms. In northern mid and high latitudes, warming is resulting in a shift from snow to rain (Bintanja & Andry, 2017; Tamang et al., 2020). In the Upper Great Lakes region, the mean annual wet-bulb temperature is increasing, and snowfall and snowfall-precipitation ratio is decreasing (Tamang et al., 2020). Rainfall in the place of snowfall impacts water resources (Knowles et al., 2006), and glacier mass balance (Perry et al., 2017; Schauwecker et al., 2017), and potentially the global energy balance (Screen & Simmonds, 2012). Observed changes in precipitation including a reduction in heavy snow cover and the shift from snow to rain impacts soil moisture, watershed hydrology, and streamflow in the Midwest and Great Lakes region (Byun et al., 2019). From a societal standpoint, precipitation processes also impact transportation safety. Hazardous wintertime events such as freezing rain result in especially dangerous conditions that affect vehicle crash risks (Tobin et al., 2021). The height of the melting level in the atmosphere influences the precipitation phase at the surface

64 (White et al., 2002; Harpold et al., 2017; Cui et al., 2020), and trends show increases in
65 melt level heights are linked to increasing rainfall and rainfall intensity as a result of sur-
66 face warming (Prein & Heymsfield, 2020).

67 Satellites provide near-global observations and provide essential quantitative pre-
68 cipitation estimates for hydrometeorological applications on instantaneous/nowcasting to
69 climate time scales. Accurate portrayals of surface precipitation phase from satellite re-
70 trievals are incredibly important, yet sometimes difficult to determine. Methods for sep-
71 arating rain and snow include radar profiles, surface measurements, and vertical profiles
72 of temperature and relative humidity. Studies show that snowfall can occur at temper-
73 atures warmer than 4°C (Auer Jr, 1974; Heymsfield et al., 2021), and freezing rain and
74 mixed precipitation can exist at temperatures well below 0°C (Stewart et al., 2015; Har-
75 pold et al., 2017). In addition, surface type influences the temperature thresholds for rain
76 and snow (Dai, 2008), and rain-snow temperature thresholds vary spatially (Jennings
77 et al., 2018). Snowflakes falling through temperatures above 0°C may not melt depend-
78 ing on the relative humidity (Matsuo & Sasyo, 1981; Heymsfield et al., 2021). Moisture
79 and pressure influence precipitation phase, and using wet bulb temperature (also referred
80 to as ice-bulb temperature below 0°C) improves rainfall/snowfall discrimination (Ding
81 et al., 2014; Behrangi et al., 2018) because the variable depends on temperature, pres-
82 sure, and relative humidity. Atmospheric data in reanalysis products including temper-
83 ature, relative humidity, wet bulb temperature, and near surface lapse rates can be used
84 with other observations including radar to determine precipitation phase at the surface.

85 In addition to measured or model-derived meteorological variables, radar profile
86 observations provide valuable information about precipitation phase. As snowflakes melt,
87 relatively large ice hydrometeors become coated by liquid water and thus can produce
88 a higher return in the reflectivity enhanced by a larger dielectric factor for liquid water
89 (Austin & Bemis, 1950). This enhanced reflectivity is referred to as the radar bright band.
90 Williams et al. (1995) classified precipitation from stratiform, mixed stratiform/convective,
91 deep convective, and shallow convective clouds using Doppler radar variables from wind
92 profilers in the tropics. White et al. (2002) developed an operational method using Doppler
93 spectra from a network of vertically profiling radars in California to identify the radar
94 bright band. Studies have explored implications for local hydrology (White et al., 2002;
95 Lundquist et al., 2008; Henn et al., 2020), glaciology (Perry et al., 2017; Schauwecker et
96 al., 2017), and microphysical differences between rain with and without a bright band
97 (Martner et al., 2008; Lin et al., 2020). Methods for identifying melting through verti-
98 cally profiling radar observations use variables including reflectivity (Cha et al., 2009),
99 Doppler velocity (Perry et al., 2017), Doppler spectra skewness (Garcia-Benadi et al.,
100 2020), and neural networks (Brast & Markmann, 2020). Weather radars employ other
101 methods using dual polarization capabilities to identify melting (Giangrande et al., 2008;
102 Matrosov et al., 2017; Ryzhkov & Zrnic, 2019).

103 Current satellite missions that provide valuable precipitation datasets include the
104 Global Precipitation Measurement (GPM) Observatory (Hou et al., 2014; Skofronick-
105 Jackson et al., 2017) and CloudSat (Stephens et al., 2008). GPM observes precip from
106 68°S to 68°N, while CloudSat observes from 82°S to 82°N. Different satellite products em-
107 ploy unique radar retrieval phase discrimination methods combining cloud/precipitation
108 profile characteristics and reanalysis products. For Cloudsat, an inflection in reflectiv-
109 ity and attenuation can indicate the bright band in stratiform rainfall (Matrosov, 2010;
110 Lebsock et al., 2020), while Liu (2008) employ a +2°C temperature threshold for snow-
111 fall/rainfall discrimination. For GPM Dual-Frequency Precipitation Radar (DPR), en-
112 hancements in the profile dual frequency ratios of reflectivity indicate bright bands (Le
113 et al., 2016; Chandrasekar & Le, 2020). However, it remains challenging to get reliable
114 precipitation measurements near the surface due to ground clutter. The satellite radar
115 blind zone – radar observations directly above the surface that are affected by ground
116 clutter - ranges from ~700 m to over 2 km above the surface depending on surface type

(e.g., ocean versus land) and topography (Casella et al., 2017; Bennartz et al., 2019; Valdivia et al., 2022). In the case of shallow snowfall, satellite radars underestimate precipitation rate and occurrence (Maahn et al., 2014; McIlhattan et al., 2020). Satellite incidence angle has also been shown to affect observations resulting in underestimation of shallow precipitation (Hirose et al., 2021). In the case of rain falling at the surface, the satellite radar blind zone also poses an obstacle, masking vertical gradients in drop size and potentially obscuring liquid precipitation entirely when the melting level is shallow. Watters et al. (2018) showed that shallow bright bands were misidentified as surface clutter in GPM DPR resulting in retrievals above the melt layer. For passive sensors, such as the GPM Microwave Imager (GMI), surface type and snow cover contribute further to challenges in phase discrimination at the surface (Skofronick-Jackson et al., 2015). Skofronick-Jackson et al. (2019) showed that using the Sims and Liu (2015) method with wet-bulb temperature and near surface lapse rates reduced differences between GPM DPR and Cloudsat surface precipitation retrievals. GPM DPR overestimates snowfall, but using 2 m wet bulb temperature from reanalyses improves phase discrimination (You et al., 2021). Also, there are ongoing updates and improvements to the GPM DPR phase discrimination and retrievals of precipitation rate (Hirose et al., 2021; Meneghini et al., 2021). New and upcoming satellite observing systems will enhance observations of clouds and precipitation and capture precipitation closer to the surface. In addition, planned satellite missions such as the Earth Clouds, Aerosol and Radiation Explorer (EarthCARE Illingworth et al., 2015) and the Atmospheric Observing System (AOS; <https://aos.gsfc.nasa.gov/>) are being designed with Doppler radar capabilities.

Ground-based radars - especially vertically pointing profiling radars - provide insights to near surface precipitation processes that may be obscured in the satellite radar blind zone. This work analyzes precipitation phase from the radar Doppler velocity by identifying and analyzing the height where ice melts to rain defined as the rain-snow level. The analysis provides insights to rain-snow levels in the context of observing near surface precipitation within the satellite radar blind zone using Doppler radar capabilities. The following questions are addressed with the ultimate goal of providing robust datasets that can be used to evaluate satellite-derived surface precipitation phase and improve the accuracy of such retrievals: How do rain-snow levels vary throughout the year? Do the macro and microphysical characteristics of rainfall events differ as a function of rain-snow level? How can these observations be coupled with ancillary measurements such as reanalyses to better address uncertainties in remote sensing retrievals of surface precipitation type? A continuous, multi-year, multi-instrument site installed at the National Weather Service (NWS) Weather Forecast Office (WFO) in Marquette, Michigan provides a unique set of observations to examine precipitation phase and these questions in the Midwest region of the United States. Section 2 describes the instrumentation and data used in this work. Section 3 outlines the methodology used to identify rain-snow levels from radar profile observations. Section 4 presents the radar rain-snow level results and the macro and microphysical characteristics of the rainfall events. Section 5 expands upon results to address applications related to satellite-based rain rate retrievals and surface phase discrimination. Section 6 concludes and summarizes key points from the analysis.

2 Instrumentation and Data

This study uses observations from a continuous, multi-year suite of instruments at Marquette, MI (MQT; Pettersen, Kulie, et al., 2020; Kulie et al., 2021; Shates et al., 2022). The MQT instrument suite is located at the MQT NWS WFO, 13 km inland of Lake Superior and 426 m above sea level. The MQT NWS provides surface meteorological measurements including air and dew point temperature (2 m) and wind speed and direction (10 m) with 5-minute resolution. In 2014, an enhanced snowfall instrument suite was installed, which includes a Micro Rain Radar and Precipitation Imaging Package. MQT

169 observations have been used to explore cold season precipitation characteristics at MQT.
170 Pettersen, Kulie, et al. (2020) examined snowfall regimes: shallow lake effect snow and
171 deep synoptically forced snow. Kulie et al. (2021) further characterized MQT snowfall
172 regimes, including enhancements of shallow and deep snowfall from the effects of orog-
173 raphy and Lake Superior. The Great Lakes Region also experiences precipitation from
174 atmospheric rivers (Slinsky et al., 2020; Mateling et al., 2021), and Mateling et al. (2021)
175 illustrated that atmospheric river events impact the MQT site and often lead to enhanced
176 precipitation rates and cold-season rain events.

177 2.1 Micro Rain Radar

178 The METEK MicroRain Radar 2 (MRR) is a 24 GHz (K band) vertically profil-
179 ing frequency-modulated, continuous wave Doppler radar (Klugmann et al., 1996). The
180 MRR is portable and relatively inexpensive, and uses relatively low power, which make
181 it useful for observing precipitation across remote regions including mountainous sites
182 and Antarctica (Kneifel et al., 2011; Schirle et al., 2019; Shates et al., 2021; Cooper et
183 al., 2022; Gorodetskaya et al., 2014). The MRR was originally deployed and evaluated
184 for measuring rainfall in remote regions (Peters et al., 2002; Maahn & Kollias, 2012). In
185 addition, MRR observations have been used in identifying melting in stratiform rain (Cha
186 et al., 2009; Brast & Markmann, 2020; Garcia-Benadi et al., 2020). The MRR observa-
187 tions were processed using the Maahn and Kollias (2012) method providing 1-minute res-
188 olution of equivalent radar reflectivity (Z_e ; dBZ), Doppler velocity (V_d ; ms^{-1}) and spec-
189 tral width (ms^{-1}). The processing also improves the sensitivity of the radar reflectivity
190 to -10 dBZ. The operating range height of the radar is 3 km above ground level (AGL)
191 and the range resolution is 100 m. Observations below 400 m AGL are removed due to
192 ground clutter contamination, and 400 m AGL is defined as the near surface height bin.
193 The stability of the MRR was assessed by comparing the 400 m AGL MRR reflectivi-
194 ties to NEXRAD radar reflectivities at approximately 400 m AGL (See Appendix A).
195 The assessment supports that the MRR is stable in time.

196 2.2 Precipitation Imaging Package

197 The Precipitation Imaging Package (PIP) is a custom NASA video imager that uses
198 a coupled bright light source and high speed camera to capture videos of shadows of falling
199 hydrometeors (Newman et al., 2009; Pettersen, Bliven, et al., 2020; Pettersen et al., 2021).
200 Image processing of these videos produce tables of hydrometeor microphysical charac-
201 teristics at 1-minute resolution, including drop size distributions (DSDs) and particle ve-
202 locity distributions (VVDs). The PIP can resolve hydrometeors ranging from 0.4 to 26
203 mm with a 0.2 mm resolution. Additional processing provides an effective particle den-
204 sity and precipitation rates in liquid water equivalent (Pettersen, Bliven, et al., 2020).
205 Additionally, the PIP can effectively discriminate precipitation phase (Pettersen et al.,
206 2021).

207 2.3 Reanalyses

208 This study incorporates reanalysis products from European Centre for Medium-
209 Range Weather Forecasts (ECMWF) ERA 5 (Hersbach et al., 2020; C3S, 2021) and the
210 NASA Modern-Era Retrospective analysis for Research and Applications MERRA-2 (Gelaro
211 et al., 2017). ERA5 has hourly temporal resolution, a spatial resolution of $0.25^\circ \times 0.25^\circ$,
212 and a vertical resolution of 37 pressure levels. MERRA-2 has a three-hourly temporal
213 resolution, a spatial resolution of $0.5^\circ \times 0.625^\circ$, and 42 vertical pressure levels. We use ver-
214 tical profiles of temperature and relative humidity at the nearest latitude and longitude
215 coordinates to the MQT site: 46.5°N , 87.5°W .

216 Vertical profiles in reanalysis products are along pressure coordinates, but must be
217 converted to height coordinates for radar profile comparisons. For MERRA-2, the edge

218 height variable (edgeH) in units of m is used. The site elevation (426 m) was subtracted
 219 from the edge heights under the assumption that layer thicknesses (Bosilovich et al., 2016)
 220 are originally calculated from sea level. The ERA5 height coordinates are calculated us-
 221 ing hydrostatic balance and the hypsometric equation (Petty, 2008) using 975 hPa as
 222 the surface level.

223 Profiles of wet bulb temperature are calculated iteratively from the profiles of tem-
 224 perature and relative humidity (Tamang et al., 2020) with the Brent (1973) optimiza-
 225 tion method. Vertical profiles of wet bulb temperature are linearly interpolated to in-
 226 crease temperature resolution to 0.01°C also improving the height resolution. The wet
 227 bulb temperature can be used to define the melt level in the profile (Stewart et al., 2015;
 228 Sankaré & Thériault, 2016; Harpold et al., 2017; Cui et al., 2020; Prein & Heymsfield,
 229 2020; Heymsfield et al., 2021).

230 3 Methods

231 As snowflakes melt to raindrops, they fall faster towards the surface (Atlas et al.,
 232 1973). This is apparent in the Doppler velocity (V_d) of a vertically profiling radar where
 233 the V_d is greater for rainfall than snowfall. In the column above the radar, the transi-
 234 tion from snow to rain is associated with a distinct V_d increase and is evident in the gra-
 235 dient of the V_d with respect to height (Williams et al., 1995; White et al., 2002; Pfaff
 236 et al., 2014; Lin et al., 2020). In this work, we define the rain-snow level (RSL) based
 237 on a peak inflection in the V_d gradient, which is where the melting is the strongest (Lin
 238 et al., 2020). The RSL generally appears below the radar reflectivity indicated bright
 239 band. In addition, the bright band height determined by the dual-frequency reflectiv-
 240 ity ratio from the GPM DPR has also been shown to agree well with melt level heights
 241 derived from V_d (Lebsock et al., 2020).

242 The rain and RSL identification starts with a threshold for precipitation occurrence
 243 of radar reflectivity greater than -10 dBZ at the 400 m AGL (Pettersen, Kulie, et al.,
 244 2020; Mateling et al., 2021; Kulie et al., 2021; Shates et al., 2021). Next, rain and snow
 245 are separated using a V_d threshold (White et al., 2002) where rain is conservatively cat-
 246 egorized as having V_d greater than 3 ms^{-1} . This surface phase identification was tested
 247 and verified with multiple snow-rain transition events using the PIP particle effective den-
 248 sity product, which accurately discriminates rain versus snow (Pettersen et al., 2021).
 249 Figure 1a shows observations from the MRR and PIP during a rain to snow transition
 250 event. Surface precipitation phase from the effective density shows a shift from rain to
 251 mixed precipitation to snow. The detection of the RSL corresponds to raining periods
 252 detected by the PIP. Additionally, Pettersen et al. (2021) show that the PIP effective
 253 density product compares well with methods described by Sims and Liu (2015) that use
 254 surface wet bulb temperature and near surface lapse rates to determine surface snow-
 255 fall probability.

256 Figure 1b contains an example of a V_d profile and corresponding V_d gradients with
 257 respect to height (the derivative of V_d with respect to height is designated as dV_d) from
 258 an April rain event. Using the peak change in the gradient of the V_d profile to detect
 259 melting has been shown effective in stratiform precipitation (Williams et al., 1995; White
 260 et al., 2002; Pfaff et al., 2014; Lin et al., 2020). White et al. (2002) defined a threshold
 261 of $-7.14 \times 10^3 \text{ s}^{-1}$ ($-1.5 \text{ ms}^{-1}/210 \text{ m}$) to flag melting in the V_d profile. For this study, the
 262 threshold value to identify the height of the RSL is $-7.5 \times 10^3 \text{ s}^{-1}$ ($-0.75 \text{ ms}^{-1}/100 \text{ m}$). The
 263 threshold was determined empirically to effectively separate profiles with and without
 264 melting in the MRR range, and accounts for the MRR range resolution (100 m). Ad-
 265 ditionally, the RSL is calculated for downward moving velocities only (toward the radar);
 266 any upward motions are ignored. For flagged rain associated with melting in the range
 267 of the radar, more than 90% of the peak dV_d magnitudes exceed the threshold. The RSL
 268 were also evaluated against NEXRAD-identified rain-snow levels for 550+ coincident min-

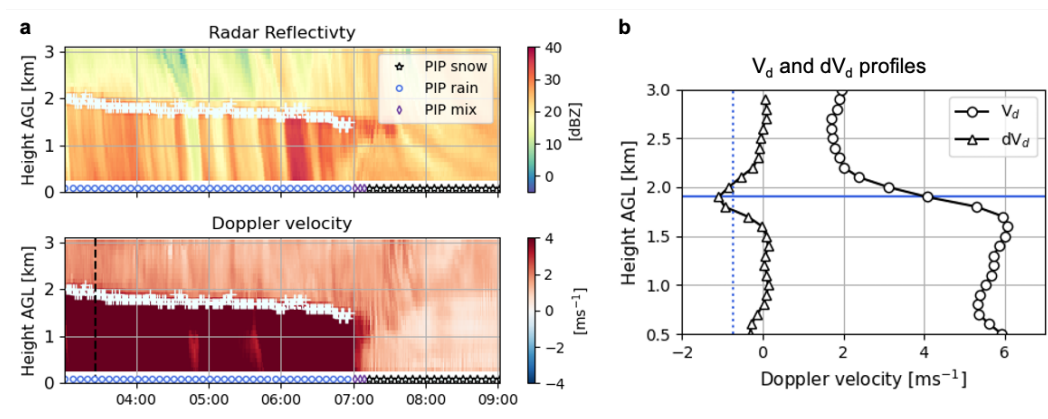


Figure 1. Methods summary and example of rain-snow level identification. (a) Radar reflectivity and Doppler velocity time series are shown for a rain to snow transition event at MQT on 10 April 2015. The rain-snow levels are plotted on the radar reflectivity and Doppler velocity as white + symbols. The PIP phase observed at the surface is superimposed on to the radar time series. The black, dashed vertical line in the Doppler velocity time series indicates the time of the profile explored in the plot to the right. (b) The V_d and dV_d are shown. The dV_d threshold is plotted as a blue, dashed vertical line. The blue, solid horizontal line shows the height of the identified rain-snow level for that minute.

269 utes of rainfall during 19 different days. The cross correlation coefficient (ρ_{HV}) from scan-
 270 ning radars can be used to identify melting (Giangrande et al., 2008; Matrosov et al.,
 271 2017; Gatlin et al., 2018; Ryzhkov & Zrnice, 2019). We used scans between 6° and 10°
 272 in order to avoid ground clutter contamination. The NEXRAD ρ_{HV} and MRR RSL are in
 273 good agreement with differences in values within the range resolution of the MRR (fig-
 274 ure not shown).

275 Rain events without a melting signature within the operating range height of the
 276 radar (3 km AGL) were flagged as undetected when the following criteria were met: the
 277 minimum V_d was greater than 3 ms^{-1} throughout the profile and continuous radar re-
 278 flectivity values were greater than -10 dBZ throughout the profile up to 3 km AGL. These
 279 rain events are likely associated with melting above 3 km AGL. The undetected cate-
 280 gory may also include instances of rainfall without a discernible rain-snow level. Warm
 281 rain or shallow convective rainfall, which are rare at this site, would not be flagged at
 282 all, as the dV_d threshold would not be met and precipitation echo tops would be too shal-
 283 low for the continuous radar reflectivity criteria.

284 In section 5, we use MRR RSL to evaluate the reanalysis derived melt levels from
 285 ERA5 and MERRA-2. The temporal resolution for ERA5 is hourly and MERRA-2 is
 286 3-hourly, while the MRR observations are one-minute resolution. To compare the ob-
 287 servations to reanalyses with different temporal resolutions, we use a 25-minute thresh-
 288 old to flag hours. For flagged RSL hours, we compute the mean RSL to represent the
 289 full hour. We then match the hours of the flagged MRR-determined RSL with the cor-
 290 responding 3-hourly MERRA-2 time resolution. The 3-hourly resolution is used to com-
 291 pare the mean MRR RSL, ERA5 and MERRA-2 hours.

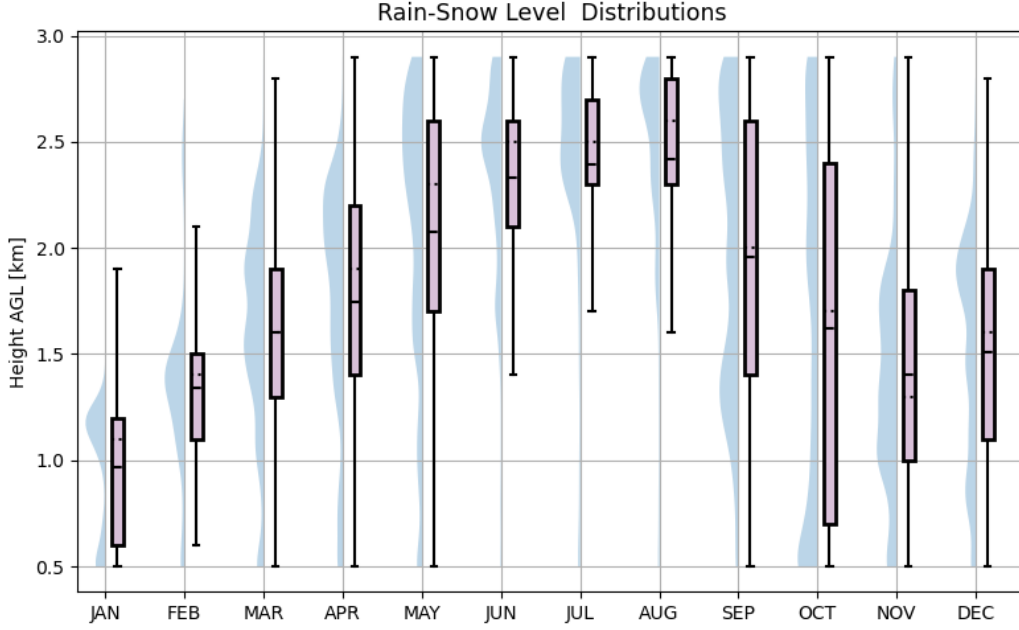


Figure 2. Distribution of rain-snow levels. The boxes include the 25th to 75th percentile of the data and the whiskers span from the 5th to the 95th percentile. The solid lines show the mean values and the black dotted line/point shows the median. To the left of each box, there are half violin plot showing the empirical distribution of the data for that month.

Table 1. Rain-snow level Summary

Height Category AGL [km]	0.6 - 1.2	1.2 - 1.8	1.8 - 2.4	2.4 - 3	undetected
Percent Occurrence	9.44%	15.6%	17.59%	22.3%	26.5%
Event hours	31	53	61	85	<i>X</i>

4 Results

4.1 Analysis of MRR rain-snow levels

The RSL at MQT vary throughout the year. Figure 2 shows the annual distribution of RSL as a box and whisker plot and half violin plots (empirical distributions of the data) for all precipitation events when a RSL is observed below 3 km AGL. The summer months (JJA) have consistently higher RSL (> 2 km AGL), with the values in July and August primarily above 2.5 km AGL. Rain-snow levels during winter months (NDJF) occur closer to the surface (RSL < 2 km AGL). The mean RSL is the lowest in January at 0.9 km AGL, while the distribution for December is the highest out of the winter months. The transition season months (MAM and SON) exhibit substantial spread in the RSL ranging from 0.5 km to 3 km AGL. May and October are the two rainiest months in MQT (See appendix table B2) and both have the largest RSL range between the 25th and 75th percentile (0.7 km to 2.4 km AGL). However, the half violin plots show that October dis-

305 distribution is concentrated below 1 km AGL, whereas the May distribution has a higher
306 distribution above 2 km AGL.

307 Loosely guided by the vertical resolutions of spaceborne radars (250 – 500 m), the
308 RSL are separated into four height ranges to assess whether macro and microphysical
309 characteristics depend on RSL: 0.6-1.2 km, 1.2-1.8 km, 1.8-2.4 km, 2.4-3 km AGL. Ta-
310 ble 1 summarizes the frequency of occurrence during the full observation period (Jan-
311 uary 2014-April 2020) for the observed height categories. During the observational pe-
312 riod, 72,290 surface rain minutes were detected by the MRR, with 53,139 flagged as con-
313 taining a rain-snow transition. For the 26.5% of occurrences without a detected tran-
314 sition, RSLs above 3 km AGL are likely. In June-September, approximately 40-65% of
315 the rainfall events did not have a discernible transition in the range of the radar (Table
316 A1). The high instance of non-detection in the summer supports that the melting oc-
317 curred above the operating range height of the radar. The 2.4-3 km height category has
318 the highest percentage of rainfall with a RSL (22.3%). The 0.6-1.2 km height category
319 has the lowest frequency of occurrence at 9.44%. The event hours listed in the summary
320 table (Table 1) show the number of hours that are represented in each category for re-
321 analysis comparisons. The order of increasing number of hours with increasing RSL matches
322 with the increasing percent occurrence for the entire observation period.

323 4.2 Macro and microphysical characteristics of rainfall

324 As snow falls and melts to rain, the radar reflectivity and Doppler velocity observed
325 by the radar changes with height. Figure 3 contains two-dimensional histograms that
326 composites all rain events observed with flagged RSL in the MRR for the separate height
327 categories. The presence of a bright band is apparent with an increase followed by a de-
328 crease in reflectivity with decreasing height for height categories (Fig. 3a-d). For RSL
329 above 1.8 km AGL, the range of snowfall reflectivities are narrower (10-20 dBZ at heights
330 above 1.8 km AGL) than for the near-surface rainfall reflectivities. Near the surface, re-
331 flectivities range from 15 dBZ to greater than 30 dBZ (Fig. 3a,b). Reflectivity gradu-
332 ally increases toward the RSL (above bright band for the reflectivity) for height cate-
333 gory 1.2-1.8 km AGL and 0.6-1.2. For height category 0.6-1.2 km AGL, the reflectivi-
334 ties of snowfall above the melting layer have a broader range from 5-18 dBZ compared
335 to the other height categories. The reflectivities near the surface occur between 10 and
336 25 dBZ for the lowest height category (Fig. 3d). Near the surface, the mean reflectiv-
337 ity values are 17.8 dBZ, 18.55 dBZ, 21.9 dBZ, and 21.79 dBZ for the four height cate-
338 gories 0.6-1.2 km, 1.2-1.8 km, 1.8-2.4 km, 2.4-3 km AGL respectively.

339 The snowfall above the RSL has a relatively narrow range of V_d values ranging from
340 0 to $\sim 2.4 \text{ ms}^{-1}$ for all height categories. Below the RSL, the V_d s increase and the range
341 in V_d broadens (Fig. 3e-h), which also corresponds to a broadening and increase in spec-
342 tral width right below the RSL (not shown). The V_d does not continue to broaden to-
343 ward the surface after the initial broadening associated with the RSL. The near surface
344 V_d s for RSL 0.6-1.2 and 1.2-1.8 km AGL range from 3-6 ms^{-1} . (Fig. 3g,h) with mean val-
345 ues of 5.2 ms^{-1} and 5.4 ms^{-1} . The near surface V_d for transitions above 1.8 km AGL have
346 the highest occurrence of values exceeding 5 ms^{-1} . The mean V_d s are 5.8 ms^{-1} and 5.8
347 ms^{-1} for the height categories 1.8-2.4 and 2.4-3 km AGL. The highest RSL category (2.4-
348 3 km AGL) has V_d s exceeding 7 ms^{-1} .

349 Figure 4 contains observations of the PIP microphysical characteristics for each RSL
350 height category. In the mean drop size distributions (DSDs), there are differences in the
351 concentrations of small drops and large drops for RSL height categories (Fig. 4a). For
352 the two RSL height categories above than 1.8 km AGL, there is a larger concentration
353 of drops with diameters between 1-2 mm than for RSL above 1.8 km AGL. The DSDs
354 for RSL below 1.8 km AGL have higher concentrations of drops greater than 2 mm. The

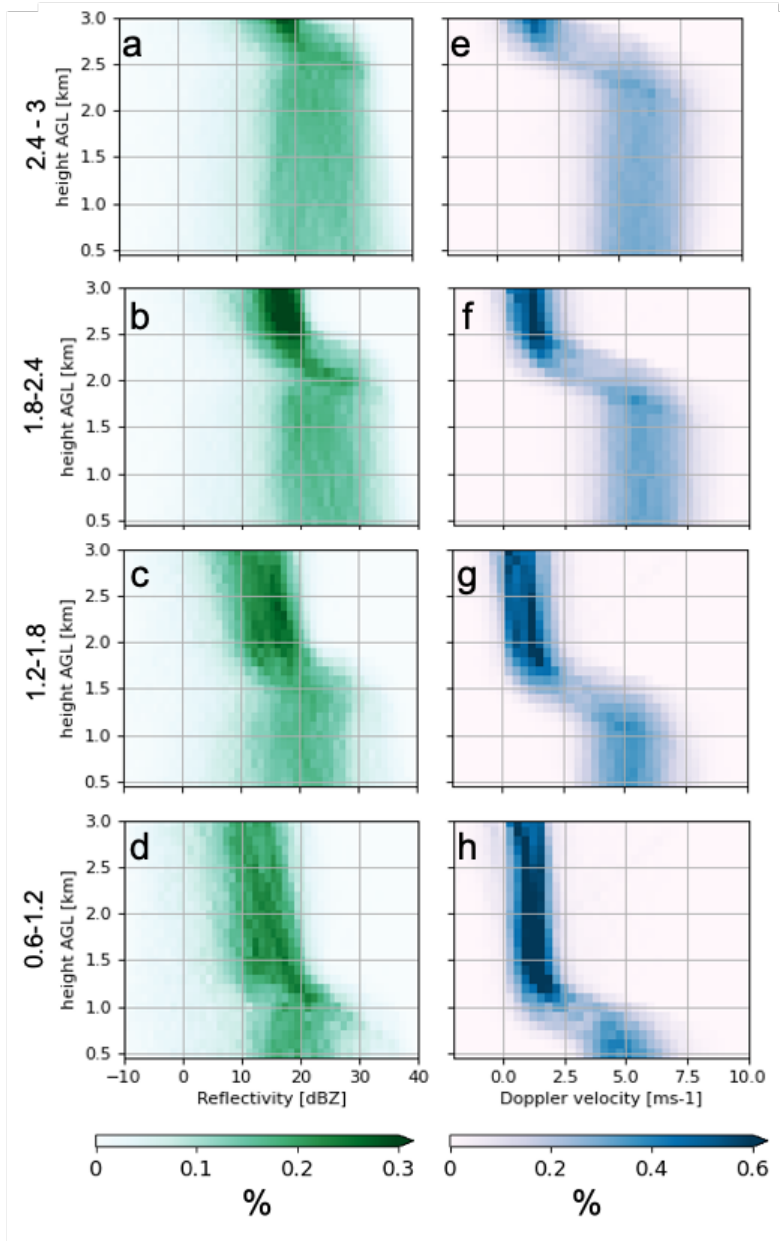


Figure 3. Two dimensional histograms of radar profiles of reflectivity and Doppler velocity from all rain events from observational period. Radar profiles are shown in subplots separated by RSL height categories: 0.6-1.2 km (a, e), 1.2 -1.8 km (b, f), 1.8-2.4 km (c, g), 2.4-3 km (d, h). The histograms are normalized by total number of observations for each height category.

355 shallowest RSL category (0.6-1.2 km AGL) has the highest concentration of drops larger than
 356 2.5 mm compared to the other height categories.

357 The mean PIP-derived fall speeds for the RSL categories are similar for drop di-
 358 ameters smaller than 2 mm (Fig. 4b), and they follow the expected curve for the termi-
 359 nal velocity of raindrops increasing drop size with increasing fall speed (Atlas et al., 1973;
 360 Atlas & Ulbrich, 1977; Uplinger, 1981). For drops larger than 2 mm, a separation in fall
 361 speeds emerges between the RSL height categories. Shallower RSL events have lower fall

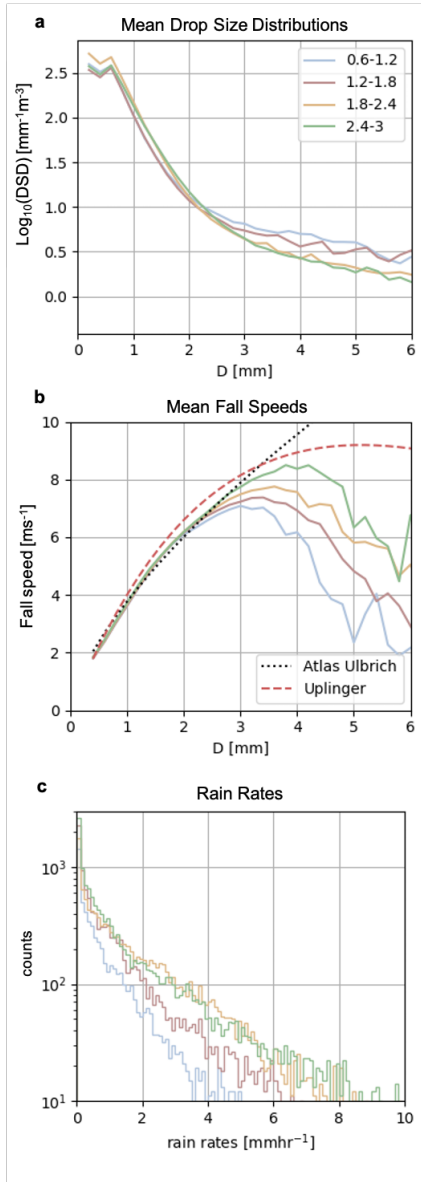


Figure 4. PIP results for RSL height categories (1.2 -1.8 km 1.8-2.4 km, 2.4-3 km AGL) including (a): mean drop size distributions, (b) mean fall speeds, (c) one dimensional histogram of rain rates. In (b), the terminal velocity as a function of drop size are included as a black, dotted line for Atlas and Ulbrich (1977), and red, dashed line for Uplinger (1981) as described by Serio et al. (2019).

362 speeds for the same equivalent diameter drops. Hydrometeors in the lowest RSL height
 363 category (0.6-1.2 km AGL) do not exceed fall speeds of 7 ms^{-1} , and fall speeds continue
 364 to decrease for particles larger than 3 mm. The PIP may be observing frozen or partially
 365 melted particles, or large deformed drops, and this is further discussed in Section 5.1.2.
 366 The highest RSL category (2.4-3 km AGL) contains drops with fall speeds greater than
 367 8 ms^{-1} .

368 Higher RSL height categories are observed to have higher rain rates (Fig. 4c). All
 369 RSL categories contain a distribution with a high concentration of low rain rates. The

370 one-dimensional histogram shows that for the lowest detected RSL (0.6-1.2 km AGL),
 371 the PIP observes rain rates up to 5 mmh^{-1} . The next height category has a higher number
 372 of observations of low rain rates, and the PIP measures rates up to 6 mmh^{-1} . Rain
 373 rates reach up to 8 mmh^{-1} for precipitation transitions between 1.8 and 2.4 km AGL,
 374 and RSL values between 2.4-3 km AGL have the highest rain rates, reaching 10 mmh^{-1} .

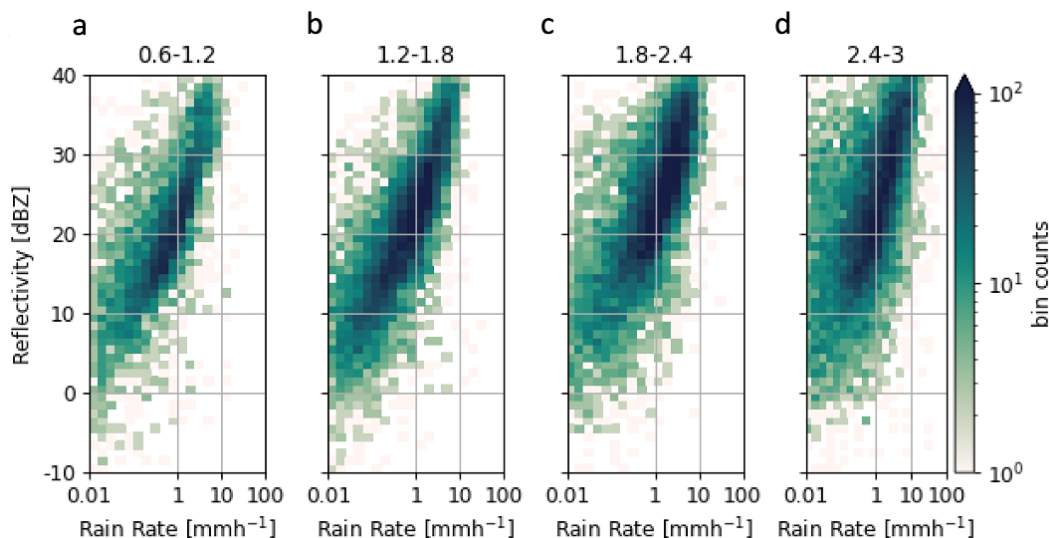


Figure 5. Two dimensional histograms of PIP rain rates in relation to MRR near surface reflectivity for separate RSL height categories AGL: (a), 1.2 -1.8 km (b), 1.8-2.4 km (c), 2.4-3 km (d). The MRR near surface reflectivity is defined at 400 m AGL because ground clutter can impact MRR observations below 400 m AGL.

375 The near-surface MRR reflectivity values and corresponding PIP rain rates are compared
 376 for the RSL height categories in the two-dimensional histograms shown in Fig. 5.
 377 For RSL above 1.8 km AGL, there are a larger number of rain rates exceeding 1 mmh^{-1}
 378 and near surface reflectivity is dominated by values greater than 20 dBZ (Fig. 5c,d). Rain
 379 events with RSL below 1.8 km AGL are dominated by rain rates less than 1 mmh^{-1} (Fig. 5a,b).
 380 The RSL between 0.6 and 1.2 km AGL have the highest concentration of near-surface
 381 reflectivities between 10 and 25 dBZ (Fig. 5a).

382 5 Discussion

383 5.1 Seasonality and the satellite radar blind zone

384 Rain-snow levels vary seasonally at MQT from January 2014-April 2020. The re-
 385 sults show that the winter months have lower RSL, occurring below 2 km AGL. Dur-
 386 ing shoulder-season months, we see the largest spread in RSL (Fig. 2). We found that
 387 for approximately 40% of the raining events with a detected RSL (27% for all rain events
 388 detected) the RSL was below 2 km AGL. Rain-snow levels respond to the seasonal change
 389 in temperature. During the cold season, most precipitation falls as snow at MQT, but
 390 Mateling et al. (2021) showed that atmospheric river events reaching the site increase
 391 the likelihood of rainfall. Surface air temperatures associated with many shallow RSL
 392 rainfall events were also near 0°C (not shown), which further underlines the challenge
 393 in using a temperature threshold to separate snow, rain-snow transitions, and freezing
 394 rain (Stewart et al., 2015) within the satellite radar blind zone.

Depending on surface type and the signal of the precipitation, the satellite radar blind zone ranges 720 m to 2 km (Casella et al., 2017; Bennartz et al., 2019), and over land in non-mountainous regions, measurements may be difficult to observe below 1.25 km. For CloudSat, attenuation from melting contributes to uncertainties with DSDs and precipitation retrievals (Matrosov, 2010). In GPM DPR, shallow melt layers result in poor phase classification in the winter (Pejcic et al., 2020), and the shallow bright band can be misidentified as ground clutter (Watters et al., 2018). In addition, scanning weather radars may also be affected by shallow melting layers, as radar beams intersecting the melting layer are affected by attenuation (von Lerber et al., 2014). Weather radars may also overshoot the melting layer due to range and beam curvature effects (Norin et al., 2015, 2017; Watters et al., 2018; Pettersen, Kulie, et al., 2020). Also, ground clutter obscures detection of shallow melting layers in weather radar (Giangrande et al., 2008).

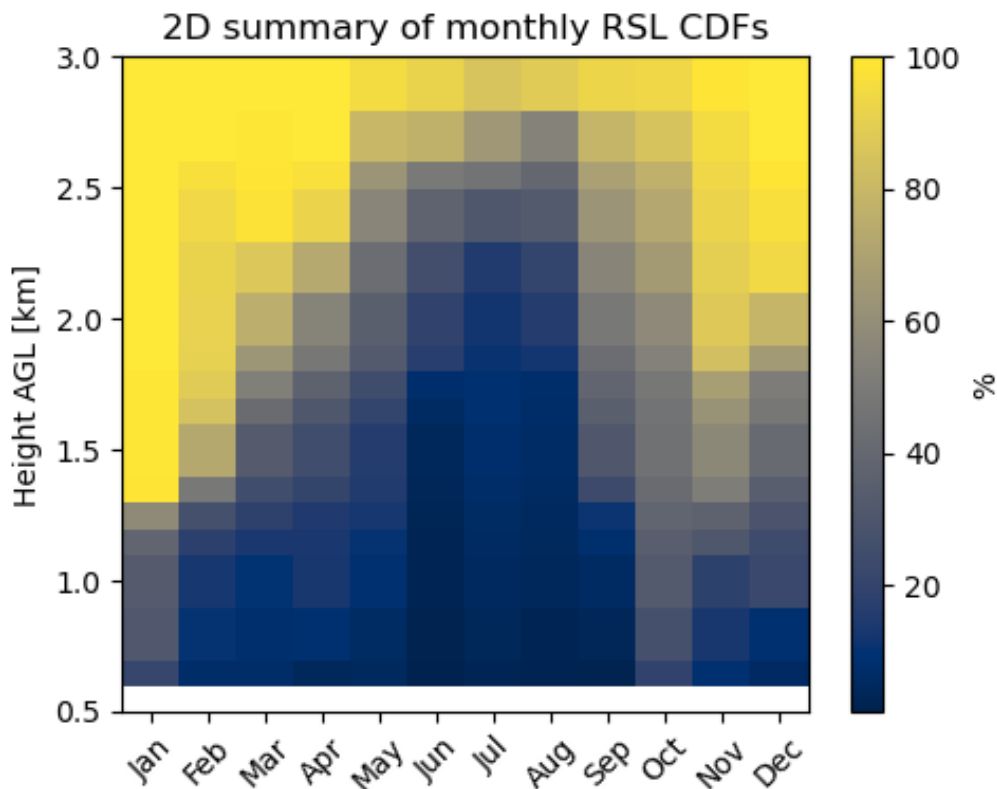


Figure 6. Monthly cumulative distribution functions (CDFs) for all detected RSL from Jan. 2014- Apr. 2020. The distributions are expressed as percents.

Figure 6 contains a two-dimensional composite of monthly cumulative distribution functions (CDFs) for the RSL. The monthly CDFs show the percentages of the RSL observed below each 100 m bin resolution for each month of the year (resolution of the MRR). The 2D CDF summary provides insights into the fraction of scenes for which the RSL may be difficult to observe through a space-based radar as a function of blind zone depth. In January, effectively 100% of the melting layers occur below 1.5 km AGL. More than 60% of the RSL in February are observed below 1.5 km AGL. In December, approximately 40% of the RSL are below 1.5 km AGL. As spring months progress towards summer months, the CDFs decrease with increasing height, indicating that there are higher RSL in the distribution even though there are some shallow transitions (Fig. 2). Beginning with Septem-

ber, the CDFs show that the melt levels are closer to the surface for a higher percentage of the observations, although the spread is still large (Fig. 2).

The results of the RSL height categories show a separation in the macro and microphysical characteristics of rainfall with RSL above and below 1.8 km AGL. The following discussion will describe the RSL as shallow for height categories below 1.8 km AGL (RSL: 0.6-1.2 km and 1.2-1.8 km AGL) and intermediate for RSL above 1.8 km AGL (RSL: 1.8-2.4 km and 2.4-3.0 km AGL). The term intermediate reflects the fact these RSL are not shallow, but are also within the range of the radar, which is limited to below 3 km AGL.

5.1.1 Intermediate rain-snow levels

Rain-snow levels above ~ 2 km AGL are likely to be correctly identified by spaceborne radars, as they are generally occurring above the blind zone, depending on surface type and presence of orography (Casella et al., 2017; Bennartz et al., 2019). Watters et al. (2018) showed that phase detection in GPM DPR was better in summer months than winter months because of the relatively higher bright bands. The MRR reflectivity profiles show that there is a notable increase in reflectivity associated with the RSL (Fig.3a,b), and retrievals using reflectivity gradients would capture the RSL. The PIP rain rates corresponding to the near-surface MRR reflectivities are concentrated greater than 1 mmh^{-1} for the intermediate height categories (Fig.5c,d). PIP observations show that these rain events also tend to have higher rain rates that exceed 6 mmh^{-1} (Fig. 4c). Correspondingly, higher melting levels have been shown to be associated with higher rain rates (Henn et al., 2020; Prein & Heymsfield, 2020).

The microphysical characteristics of intermediate height categories suggest precipitation processes occurring below the RSL. The surface-based observations of DSDs for intermediate height categories contain a higher concentration of small drops (effective diameters between 1 and 2 mm). The high concentration of small drops suggests the occurrence of drop breakup as the rain drops fall below the melt level. As the raindrops fall, they collide and break up resulting in more and smaller drops (List & Gillespie, 1976). Prein and Heymsfield (2020) describe that increasing melt levels results in an increase in warm rain processes including collision and coalescence. The high number concentration of small drops is consistent with heavier rainfall associated with a higher melt level. Other in-situ or remote sensing measurements would be needed to further explore the processes occurring as the drops fall.

5.1.2 Shallow rain-snow levels

Rain-snow levels below 1.8 km AGL may pose a challenge for spaceborne remote sensing retrievals of rain rate, due the likelihood of occurring within the satellite radar blind zone (Casella et al., 2017; Watters et al., 2018; Bennartz et al., 2019; Pejic et al., 2020). The occurrence of RSL is also valuable to assess in a warming climate with a shift from snow to rain in northern latitudes (Tamang et al., 2020) due to increasing melt level heights (Prein & Heymsfield, 2020). In addition, melting heights decrease with increasing latitude (Lundquist et al., 2008; Cannon et al., 2017), which suggests that changes from snowfall to rainfall in high latitudes may be challenging to observe within the satellite radar blind zone.

During the shallow RSL events, the MRR reflectivities near the surface range from 10 to greater than 20 dBZ. The reflectivity of the snowfall above the melt level remains below 20 dBZ (Fig. 3c,d). Above the RSL, the MRR reflectivity two-dimensional histograms show that the reflectivities associated with snowfall steadily increase with decreasing height. While the radar reflectivity magnitude is likely affected by attenuation above the melting level, the steady increase with decreasing height may suggest aggre-

466 gation processes (Field, 2000; Shates et al., 2021) prior to melting. Dolan et al. (2022)
467 explored microphysical processes of precipitation cases through dual-polarized scanning
468 radar observations; in regions where the snowflake habit above the bright band was iden-
469 tified as aggregates there was a steady increase in reflectivity above the bright band. Also,
470 snowfall characteristics such as snow density are useful for melting layer models in quan-
471 titative precipitation estimation with weather radars (von Lerber et al., 2014). The range
472 of near-surface reflectivities for these RSL rain events have lower values compared to the
473 intermediate RSL height categories, and the PIP observed rain rates are concentrated
474 below 1 mmh^{-1} (Fig. 5a,b).

475 Proximity of the RSL to the surface impacts the DSDs and fall speeds of hydrom-
476 eteors. The DSDs for the shallow RSL height categories contain a larger concentration
477 of drops with diameters greater than 3 mm compared to the intermediate RSL height
478 categories, and even drops as large as 6 mm are observed (Fig. 4a). The occurrence of
479 these larger hydrometeors is consistent with there being less time and distance for the
480 drops to break up into smaller drops, as the melt level is much closer to the ground (List
481 & Gillespie, 1976; Yuter et al., 2006; Stewart et al., 2015). Gatlin et al. (2018) showed
482 that lower and thicker melting layers resulted in larger rain drops in observed DSDs. The
483 PIP also observed that fall speeds start to decrease for drops larger than 3 mm (decreas-
484 ing from 6 ms^{-1} to less than 4 ms^{-1}). One possibility is that the PIP is observing large
485 deformed droplets where the droplet deformation is affecting fall speeds (Wang & Prup-
486 pachter, 1977). Yuter et al. (2006) showed the occurrence of large rain drops (effective
487 diameters $> 6 \text{ mm}$) in mixed precipitation events using PARSIVEL disdrometer mea-
488 surements. These large drops were formed from aggregates that had melted, but did not
489 have time or distance to break up. Also, larger hydrometeors with the lower fall speeds
490 may suggest that some of these shallow RSL events contain mixed precipitation that is
491 reaching the surface. The habit of the ice crystals above the melting layer can also in-
492 fluence the distance required to fully melt ice particles (Sankaré & Thériault, 2016; Stew-
493 art et al., 2015), and the mass of the snowflakes impacts the DSDs of the raindrops (Fujiyoshi
494 & Muramoto, 1996; Dolan et al., 2022). Lee et al. (2020) also found that the microphys-
495 ical characteristics of snowfall above the bright band influenced the size and concentra-
496 tions of raindrops at the surface. Above the melt level, the increasing reflectivity with
497 decreasing height suggests that many of these rain events may have snow aggregation
498 occurring aloft (Field, 2000; Shates et al., 2021; Dolan et al., 2022) particularly as the
499 temperature increases towards melting (Lamb & Verlinde, 2011) leading to potentially
500 large, partially melted aggregates/wet snow reaching the surface.

501 5.2 Remote Sensing Applications

502 5.2.1 Z-R Relationships

503 In order to obtain a precipitation rate from a radar reflectivity value, it is neces-
504 sary to use a reflectivity (Z) to rain rate (R) relationship. A Z-R power law relationship
505 and coefficients are influenced by the microphysical characteristics of rainfall including
506 the number density, size and fall speeds of rain drops (Atlas et al., 1973; Steiner et al.,
507 2004). Satellite radar precipitation retrievals used with GPM DPR depend on precip-
508 itation phase discrimination to assume a DSD for rain or particle size distribution for
509 snowfall including stratiform versus convective assumptions (Skofronick-Jackson et al.,
510 2019). There are differences in stratiform and convective rainfall microphysical charac-
511 teristics that affect precipitation retrievals (Bringi et al., 2003; Steiner et al., 2004). In
512 addition, Martner et al. (2008) and Lin et al. (2020) report differences in the Z-R rela-
513 tionships between bright band and non bright band stratiform rainfall due to microphys-
514 ical processes (collision and coalescence only versus melting snowflakes grown through
515 ice processes).

516 From the near-surface MRR reflectivity values and PIP rain rates, we are able to
 517 obtain empirically-derived Z-R relationships. Figure 7 shows operational Z-R relation-
 518 ships, empirical RSL Z-R relationships, and mean PIP rain rates for MRR reflectivity
 519 bins. The operational Z-R include: $Z = 130R^2$ Cool Season (east) Stratiform, $Z = 200R^{1.6}$
 520 Marshall Palmer Stratiform, $Z = 300R^{1.4}$ Summer Deep Convective (NWS, 2015). These
 521 specific Z-R relations are applied to NEXRAD observations, which are S-band (~ 10 cm
 522 wavelength). The empirical MRR-PIP Z-R are $Z = 133R^{2.1}$, $Z = 83R^{2.5}$, $Z = 50R^{2.7}$,
 523 $Z = 101R^{2.2}$ for RSL height categories 0.6-1.2, 1.2-1.8, 1.8-2.4, 2.4-3 km AGL respectively.
 524 While the MRR and NEXRAD do not operate at the same frequency, both mostly ob-
 525 serve liquid precipitation in the Rayleigh scattering regime. Possible non-Rayleigh ef-
 526 fects for the K-band radar observations are likely limited to very intense precipitation
 527 events that are rarely observed at MQT, especially for stratiform rainfall with relatively
 528 low melting levels. The mean rain rates from the PIP and the corresponding Z-R curves
 529 for the shallow RSL height categories (RSL < 1.8 km AGL) are distinct from the Mar-
 530 shall Palmer Z-R relationship for stratiform rain, but match well with the Z-R relation-
 531 ship used by the NWS at MQT, the cool season (east) stratiform Z-R (Fig. 7a,b). The
 532 fall speeds and the DSDs suggest the presence of some wet snow (Fig. 4a,b), but the Z-
 533 R is still effective for these shallow RSL (e.g., Licznar and Krajewski (2016) showed that
 534 rain and rain with wet snow Z-R resemble each other).

535 Figure 7c,d shows that the PIP mean rain rates and the Z-R relationships for the
 536 intermediate RSL height categories (RSL > 1.8 km AGL) do not match the existing Z-
 537 R relationships used for cool season stratiform rain, nor the Marshall Palmer stratiform
 538 rain, nor deep convective rain used at the Chicago, Illinois NWS NEXRAD radar (KLOT).
 539 The two intermediate RSL height categories (1.8-2.4 km and 2.4-3 km) also have differ-
 540 ent Z-R relationships. The rain rates for RSL 2.4-3.0 km AGL have higher rain rates than
 541 those between 1.8-2.4 km for a reflectivity range of 15 and 25 dBZ. However, rain rates
 542 for reflectivities greater than 25 dBZ are higher RSL between 1.8-2.4 km. The unique
 543 Z-R relationships are likely a result of the distinct microphysical characteristics (e.g., drop
 544 size distributions; Fig. 4a). The DSDs and Z-R relationships suggest that accounting for
 545 the height of the melting level may be important for radar retrievals of precipitation.

546 5.2.2 Evaluation of profile wet bulb temperature

547 Reanalysis products are commonly used with satellite radar observations to deter-
 548 mine surface precipitation phase and retrieve snow or rain rates (e.g., Liu, 2008; Skofronick-
 549 Jackson et al., 2019; Lebsock et al., 2020; You et al., 2021). The CloudSat precipitation
 550 products use reflectivity attenuation to separate convective and stratiform precipitation,
 551 and the melting (freezing) level to separate solid and liquid precipitation (Lebsock et al.,
 552 2020). The ECMWF temperature and humidity profiles are used for the melt layer model
 553 in CloudSat products (Haynes et al., 2009). Vertical profiles of temperature and rela-
 554 tive humidity from reanalysis products provide these ancillary data. Here, we define re-
 555 analysis melt levels (ML) at the 0°C , 0.5°C and 1°C isotherms using profiles of wet-bulb
 556 temperature (T_w) calculated from ERA5 and MERRA-2 temperature and relative hu-
 557 midity profiles. The number of hours included from each RSL height category in this anal-
 558 ysis are outlined in Table 1. The MRR RSL and ERA5 ML are matched up with the 3-
 559 hourly resolution of MERRA-2 ML.

560 The vertical structure of temperature during a precipitation event largely controls
 561 the surface phase (Stewart et al., 2015; Sims & Liu, 2015; Harpold et al., 2017). The T_w
 562 profile (i.e. ML) provides additional information for phase discrimination by identify-
 563 ing the onset of melting (Fig. 8). Figure 8(a-c) contains scatter plots comparing the MRR
 564 RSL and the ML at T_w of 0°C , 0.5°C and 1°C . There is high correlation between the MRR
 565 RSL and ML for all three of the T_w . Generally, the RSL occur below the ML, which is
 566 consistent with the fact that the snow particles gradually melt through the melt layer,
 567 and the distance to fully melt depends on the microphysical characteristics of the snow-

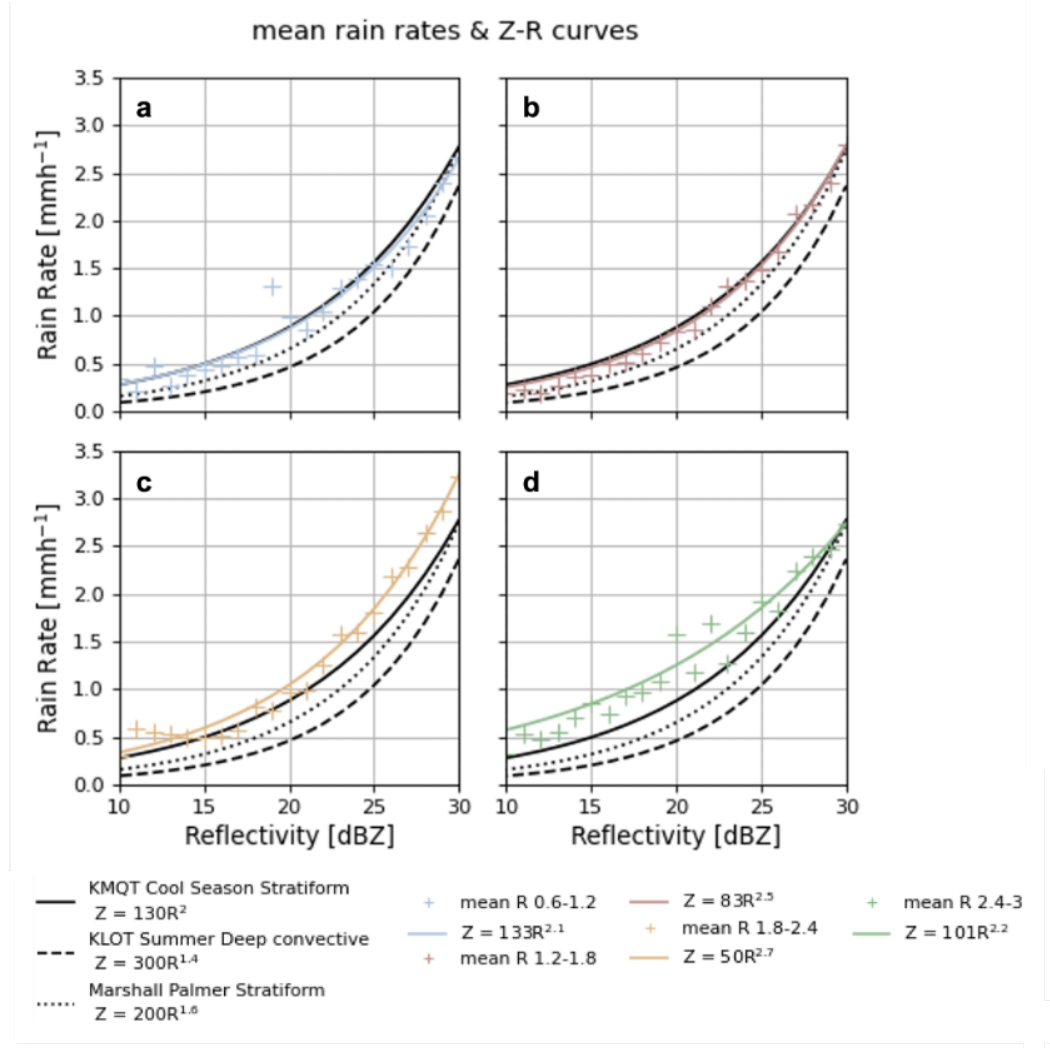


Figure 7. Z-R curves calculated from near surface MRR reflectivity and PIP rain rates for each height category 0.6-1.2 km (a), 1.2-1.8 km (b), 1.8-2.4 km (c), 2.4-3 km (d). The mean rain rates are calculated for 21 reflectivity bins ranging from 10 to 30 dBZ. The Z-R curves were obtained from the the mean rain rates between 10 and 30 dBZ. In this reflectivity range, there were a minimum of 100 rain rates (minutes) per reflectivity bin. The mean rain rates and corresponding Z-R relations are compared to Z-R relations used with NWS Doppler weather radars (WSR-88D): Marshall Palmer Stratiform, Cool Season Stratiform at Marquette, MI (KMQT), and Summer Deep Convective at Chicago, IL (KLOT).

568 fall (White et al., 2002; Stewart et al., 2015). The mode differences between the reanalysis ML and MRR RSL (reanalysis ML - MRR RSL) at the 1°C ML are 0 m for MERRA2
 569 and 100 m for ERA5, respectively. For the 0.5°C and 1°C MLs, there are an increasing
 570 number of points above the one-to-one line indicating that some of the reanalysis ML
 571 are flagged below the RSL (Fig.8b,c). At the 0.5°C ML, both ERA5 and MERRA-2 have
 572 mode differences of 200 m. Compared to the 0°C ML, the points for the 0.5°C and 1°C
 573 ML are closer to the one-to-one line for both reanalysis ML. The mode differences for
 574 MERRA-2 0°C range between 200-400 m, while the mode for the ERA5 0°C difference
 575 is 300 m. ERA5 has a higher Pearson correlation coefficient than MERRA-2 between
 576

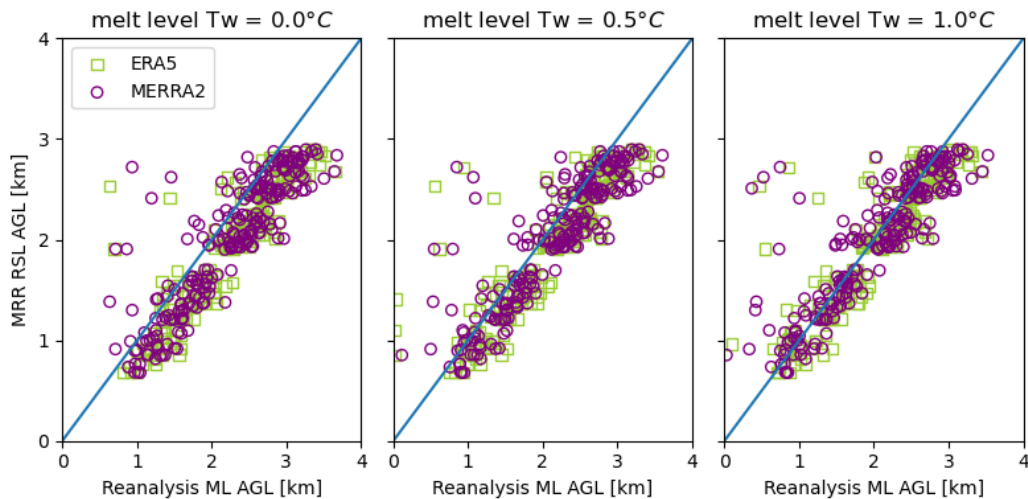


Figure 8. Scatter plots of melt levels from ERA5 and MERRA-2 reanalyses against MRR rain-snow levels. The one-to-one line is shown in blue. The subplots compare MRR RSL and the height in the profile where the wet bulb temperature is 0°C (a), 0.5°C (b) and 1°C (c). When there is a temperature inversion in the profile resulting in multiple instances of 0°C , 0.5°C and 1°C , then the highest occurrence represents the melt level. Pearson correlation coefficients between the RSL and ML from ERA5 and MERRA-2 are shown in each plot.

577 the MRR RSL and the ML (≥ 0.88), but the correlation is still high for MERRA-2
 578 for all of the ML (≥ 0.85). In general, the RSL and ML appear to agree the most at T_w of
 579 1°C for ERA5 and MERRA-2.

580 Knowing how the RSL (or reflectivity bright band height) compare to the melting
 581 level is valuable for forecasting models (Henn et al., 2020) and for satellite precip-
 582 itation retrievals (Sims & Liu, 2015; Lebsack et al., 2020). For nineteen vertically pro-
 583 filing radars on the west coast of the US, there was a ± 250 m bias between the modeled
 584 melt level (temperature of 0°C) and the radar detected bright band (Henn et al., 2020).
 585 Cui et al. (2020) showed that surface $T_w = 0.5^{\circ}\text{C}$ was the best threshold for separating
 586 rain and snow along mountain-sides. Lundquist et al. (2008) showed that there was a
 587 difference of -400 to 200 m between the radar snow level and the surface rain-snow tran-
 588 sition, but the difference varied between locations. At a mountainous site and coastal
 589 site in South Korea, Cha et al. (2009) found the error between the bright band height
 590 and radiosonde freezing level height was 329 m and 367 m, respectively. On average, White
 591 et al. (2002) showed the rawinsonde melting level was 192 m above the radar bright band.
 592 Cannon et al. (2017) investigated space-based bright band heights from GPM DPR with
 593 MERRA-2 freezing levels over the west coast of the US and over the eastern Pacific for
 594 atmospheric river events, and found that there was good agreement with a mean differ-
 595 ence of 356 m. In the same study, Cannon et al. (2017) found that the mean absolute
 596 error between GPM-DPR bright band heights and the ground-radar network was 284
 597 m. Schauwecker et al. (2017) compared reanalysis freezing levels to MRR snow level heights
 598 in the tropical Andes, and that MRR-derived levels were 240 m (220 m) below MERRA-
 599 2 (ERA-Interim) reanalysis levels. While these numerous studies use different methods
 600 in identifying melting in the radar and defining melting levels (dry bulb vs wet bulb tem-
 601 perature), our results are consistent with the difference between the RSL and ML from
 602 previous studies.

6 Conclusions

This study illustrates the annual distribution of rain-snow levels over Marquette, Michigan from January 2014 to April 2020, and the associated micro and macro physical characteristics of rainfall at the surface. Additionally, applications of RSL height categories are assessed against Z-R relationships and retrieval assumptions using reanalysis data products. The work combines ground-based vertically profiling radar, surface video disdrometer measurements, and reanalysis products for analyses of the rainfall characteristics as a function of RSL.

Vertically profiling Doppler radar observations were used to identify RSL throughout the year. The results illustrate a seasonal cycle in the height of the RSL with shallow RSL (below 1.8 km AGL) occurring in winter months and intermediate RSL (above 1.8 km AGL) in summer months. Seasonal transition months, for example May and October, showed substantial spread in RSL, ranging from below 1 km AGL and up to 3 km AGL. The shallow RSL in winter, spring and fall (particularly below 1 and 1.5 km AGL) may be challenging to detect using current space-based radar observations, while future missions should consider optimizing radar capabilities to more effectively identify shallow melt layers. These results highlight a need to investigate satellite bright band height and thickness in winter and seasonal transition months over mid-latitude ground-based sites. In addition, the shallow RSL could potentially be missed or impact observations by ground-based scanning weather radars. Understanding the signature of melting in Doppler radar profiles is relevant for future satellite observing systems including EarthCARE and AOS, which will be able to detect vertical motions in clouds and precipitation with Doppler capabilities. Future studies could continue to explore rain-snow levels in the Great Lakes Region with the MRR, NEXRAD weather radar at MQT, GPM DPR bright band heights, CloudSat rain products, and upcoming missions.

Near-surface radar observations and microphysical characteristics show differences for rain with shallow versus intermediate RSL. Intermediate RSL rainfall have higher near-surface reflectivity and Doppler velocity values. Microphysical characteristics show that DSDs have larger concentrations of small drops (effective diameter < 2 mm) and higher rain rates for intermediate RSL. For the shallow RSL, there are relatively more large hydrometeors (effective diameter > 3 mm) in the DSDs, but slower fall speeds indicating that these rain events may also include partially melted snowflakes (mixed-phase precipitation) or large deformed drops.

From the PIP and MRR observations, we empirically derived and compared the reflectivity to rain rate (Z-R) relations for rainfall from different RSL height categories. For both shallow RSL categories (< 1.8 km AGL), the Z-R curves are similar to the Z-R relation used for the NWS S-Band weather radar (KMQT) in cool season stratiform rain. The empirically derived Z-R curves for the intermediate height categories (RSL > 1.8 km AGL) were distinct from cool season stratiform rain, the Marshall Palmer stratiform rain, and also deep convective Z-R relations used for multiple NWS radars. The operational Z-R curves indicate that the relations are underestimating rainfall from the intermediate RSL.

This study explored reanalysis-derived melt levels associated with rainfall at MQT. Profiles of wet-bulb temperature were derived from MERRA-2 and ERA5 profiles of temperature and relative humidity to obtain melt levels at 0°C , 0.5°C and 1°C isotherms. We compare rain-snow levels to reanalysis melt levels, and show especially high agreement heights at 0.5°C and 1°C .

Rain-snow levels were investigated at a site in the Upper Great Lakes Region with implications for satellite detectability of rainfall near the surface. Shallow RSL are likely to be particularly challenging for satellite radars to detect and may be an increasing area of interest with the warming climate and a shift from snow to rain in the mid and high

654 latitudes. In addition, impactful precipitation events such as atmospheric rivers are re-
 655 sponsible for warm, intense precipitation in the Midwest and may be further linked to
 656 rain in the cold seasons. The insights presented in this work are valuable for the plan-
 657 ning and designing any future satellite radars in consideration of the satellite radar blind
 658 zone.

659 Appendix A Micro Rain Radar and NEXRAD

660 The radar reflectivity values from the MRR and NEXRAD are compared for 7 rain
 661 events (1 per year) from Jan. 2014 - Apr. 2020. The MRR is frequently used in remote
 662 locations for studying precipitation without ways to assess how the radar performs over
 663 time, and this comparison allows us to assess the stability of the MRR over time. Re-
 664 flectivities from the 400 m AGL height bin are used from the MRR. To obtain NEXRAD
 665 observations at a similar height bin, we use reflectivities in the 2.4° elevation scan at a
 666 range of 10 km from the radar. The horizontal scans from the NEXRAD do not include
 667 observations directly above the MRR because the MRR is adjacent (50 m) to the weather
 668 radar and is in the radar cone of silence. It is also important to note that the NEXRAD
 669 observations are from a horizontal volume scan and will include spatial differences in pre-
 670 cipitation (which is why the distributions are not a one-to-one match). To work with the
 671 NEXRAD observations, we used the Python Atmospheric Radiation Measurement (ARM)
 672 Radar Toolkit Py-ART (Helmus & Collis, 2016). Importantly, the distributions from the
 673 respective radars indicate that the MRR calibration is stable over the 7 year period and
 674 the reflectivity values do not drift (Fig. A1) In addition, the reflectivities from the two
 675 radars are comparable suggesting that the MRR reflectivities are largely unbiased. Ta-
 676 ble A1 shows that the median reflectivities for the events are similar for the MRR and
 677 NEXRAD. For most events, the difference between the radar medians are within 2 dB
 678 of each other.

Table A1. Median reflectivity values for each event for MRR and NEXRAD

event	MRR	NEXRAD
7 June 201422-24 UTC	18.75	16.5
30 May 20151-6 UTC	19.36	17.5
4 June 201613-18 UTC	26.37	24.5
29 June 20170-2 UTC	19.82	19.0
8 October 201814-22 UTC	18.73	18.5
10 June 20197-10 UTC	17.98	17.0
4 April 20204-9 UTC	20.37	19.0

679 Appendix B Rain summary

680 This section contains tables for occurrence and minutes for each month during the
 681 study period. Table B1 shows percent of rain per month where melting was not detected
 682 and melting likely occurred above 3 km AGL. Table B2 summarizes the total number
 683 of minutes for rain per month observed Jan. 2014-Apr. 2022 for RSL and rain with un-
 684 detected RSL. These total minutes do not include shallow convective rainfall.

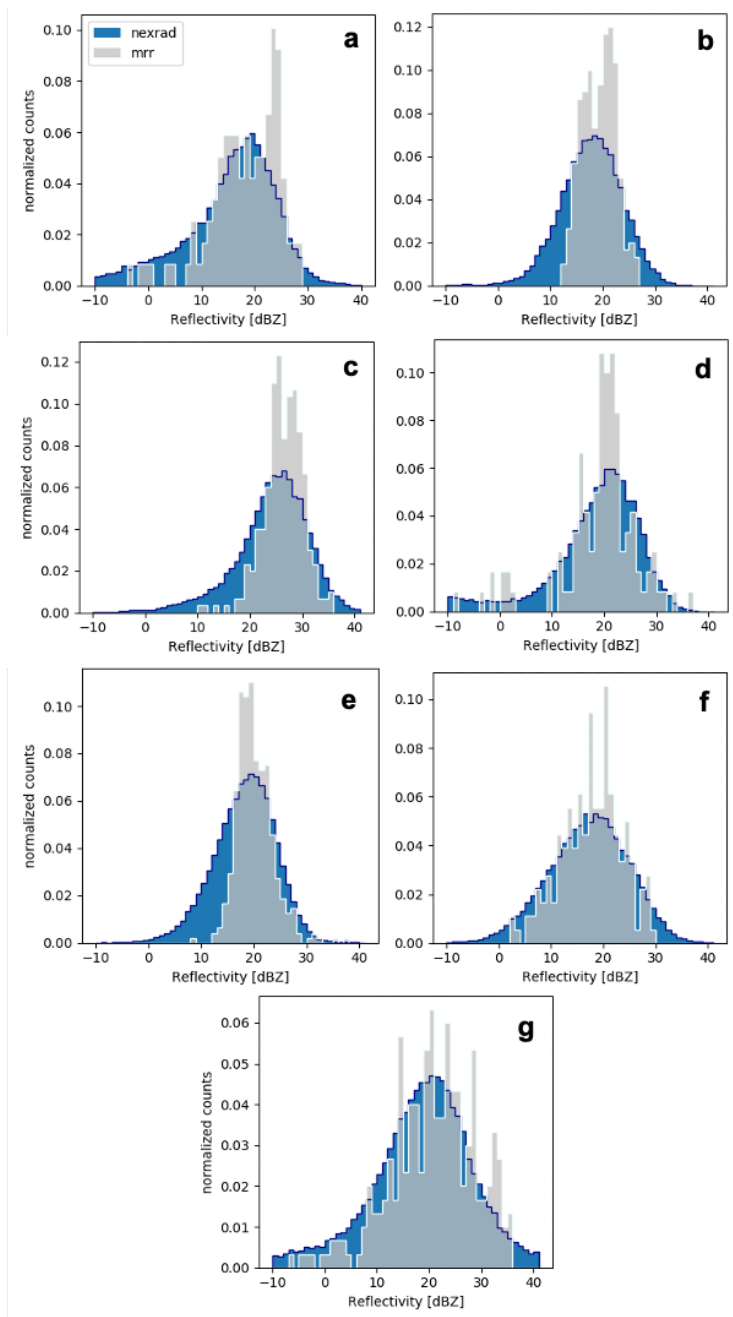


Figure A1. Normalized distributions of radar reflectivities from the NEXRAD and MRR at MQT. MRR reflectivities are at 400 m AGL, and the NEXRAD reflectivities are from the 2.4° elevation scan at 10 km range from the radar. Each distribution is from a different example event per year during within the observation period: (a) 7 June 2014, 22-24 UTC; (b) 30 May 2015, 1-6 UTC; (c) 4 June 2016, 13-18 UTC; (d) 29 June 2017, 0-2 UTC; (e) 8 October 2018, 0-5 UTC; (f) 10 June 2019, 7-10 UTC; (g) 4 April 2020, 4-9 UTC.

Appendix C Open Research

Ground-based remote-sensing observations from the Micro Rain Radar and Precipitation Imaging Package hosted at the Marquette, MI National Weather Service Of-

Table B1. Rain occurrence with undetected RSL

JAN	0.00 %
FEB	0.00 %
MAR	2.26 %
APR	1.99 %
MAY	12.18 %
JUN	47.23 %
JUL	66.89 %
AUG	55.72 %
SEP	43.61 %
OCT	17.26 %
NOV	7.75 %
DEC	0.09 %

^a Undetected RSL January 2014-April 2020.**Table B2.** Total rain minutes per month

JAN	887
FEB	1238
MAR	2789
APR	6898
MAY	11099
JUN	9298
JUL	5008
AUG	6989
SEP	8476
OCT	11617
NOV	3343
DEC	4648

^a Includes rain with and without a detected RSL.

688 fice have been uploaded to an online data repository (doi: 10.5281/zenodo.7325232). NEXRAD
689 data for Marquette were accessed August 2022 and were downloaded from the NOAA
690 National Centers for Environmental Information. The Python Atmospheric Radiation
691 Measurement (ARM) Radar Toolkit Py-ART was used to work with NEXRAD obser-
692 vations (doi: 10.5334/jors.119). ERA5 data were downloaded from the Copernicus Cli-
693 mate Data Store (CDS) and were accessed in February 2022. MERRA-2 data were down-
694 loaded from the NASA Goddard Earth Sciences Data and Information Services Center
695 and were accessed in February 2022.

Acknowledgments

We thank the Marquette National Weather Service office for their continued support in hosting instruments and sharing meteorological data. We thank Dr. David Wolff and Dr. Larry Bliven and the NASA Goddard Flight Center for the use of the MicroRain Radar and the Precipitation Imaging Package at the Marquette Weather Service Forecast Office. We also thank Aronne Merrelli for sharing python code to perform the Brentq optimization method needed to calculate wet-bulb temperature. Neither the European Commission nor ECMWF is responsible for any use that may be made of the Copernicus information or data it contains. The views, opinions, and findings contained in this paper are those of the authors and should not be construed as an official National Oceanic and Atmospheric Administration or U.S. government position, policy, or decision. This work was funded by NASA and NOAA projects: 80NSSC21K1592, 80NSSC20K0982, NNX12AQ76G, 80NSSC18K0701, 80NSSC19K0712, 80NSSC21K0931, NA21OAR4590367.

References

- Atlas, D., Srivastava, R., & Sekhon, R. S. (1973). Doppler radar characteristics of precipitation at vertical incidence. *Reviews of Geophysics*, *11*(1), 1–35.
- Atlas, D., & Ulbrich, C. W. (1977). Path-and area-integrated rainfall measurement by microwave attenuation in the 1–3 cm band. *Journal of Applied Meteorology and Climatology*, *16*(12), 1322–1331.
- Auer Jr, A. H. (1974). The rain versus snow threshold temperatures. *Weatherwise*, *27*(2), 67–67.
- Austin, P. M., & Bemis, A. C. (1950). A quantitative study of the bright band in radar precipitation echoes. *Journal of Atmospheric Sciences*, *7*(2), 145–151.
- Behrangi, A., Yin, X., Rajagopal, S., Stampoulis, D., & Ye, H. (2018). On distinguishing snowfall from rainfall using near-surface atmospheric information: A comparative analysis, uncertainties and hydrologic importance. *Quarterly Journal of the Royal Meteorological Society*, *144*, 89–102.
- Bennartz, R., Fell, F., Pettersen, C., Shupe, M. D., & Schuettemeyer, D. (2019). Spatial and temporal variability of snowfall over greenland from cloudsat observations. *Atmospheric Chemistry and Physics*, *19*(12), 8101–8121.
- Bintanja, R., & Andry, O. (2017). Towards a rain-dominated arctic. *Nature Climate Change*, *7*(4), 263–267.
- Bosilovich, M., Lucchesi, R., & Suarez, M. (2016). *Merra-2: File specification gmao office note no. 9 (version 1.1)*. GMAO Greenbelt, Maryland.
- Brast, M., & Markmann, P. (2020). Detecting the melting layer with a micro rain radar using a neural network approach. *Atmospheric Measurement Techniques*, *13*(12), 6645–6656.
- Brent, R. P. (1973). *Algorithms for minimization without derivatives, chap. 4*. Prentice-Hall, Englewood Cliffs, NJ.
- Bringi, V., Chandrasekar, V., Hubbert, J., Gorgucci, E., Randeu, W., & Schoenhuber, M. (2003). Raindrop size distribution in different climatic regimes from disdrometer and dual-polarized radar analysis. *Journal of the atmospheric sciences*, *60*(2), 354–365.
- Byun, K., Chiu, C.-M., & Hamlet, A. F. (2019). Effects of 21st century climate change on seasonal flow regimes and hydrologic extremes over the midwest and great lakes region of the us. *Science of the Total Environment*, *650*, 1261–1277.
- C3S. (2021). Era5: Fifth generation of ecmwf atmospheric reanalyses of the global climate. *Copernicus Climate Change Service Climate Data Store (CDS), date of access = March 2021*.
- Cannon, F., Ralph, F. M., Wilson, A. M., & Lettenmaier, D. P. (2017). Gpm satellite radar measurements of precipitation and freezing level in atmospheric rivers: Comparison with ground-based radars and reanalyses. *Journal of*

- 749 *Geophysical Research: Atmospheres*, 122(23), 12–747.
- 750 Casella, D., Panegrossi, G., Sandò, P., Marra, A. C., Dietrich, S., Johnson, B. T., &
751 Kulie, M. S. (2017). Evaluation of the gpm-dpr snowfall detection capability:
752 Comparison with cloudsat-cpr. *Atmospheric Research*, 197, 64–75.
- 753 Cha, J.-W., Chang, K.-H., Yum, S. S., & Choi, Y.-J. (2009). Comparison of the
754 bright band characteristics measured by micro rain radar (mrr) at a mountain
755 and a coastal site in south korea. *Advances in Atmospheric Sciences*, 26(2),
756 211–221.
- 757 Chandrasekar, V., & Le, M. (2020). Dpr dual-frequency precipitation classification.
758 In *Satellite precipitation measurement* (pp. 193–210). Springer.
- 759 Cooper, S. J., L’Ecuyer, T. S., Wolff, M. A., Kuhn, T., Pettersen, C., Wood, N. B.,
760 ... others (2022). Exploring snowfall variability through the high-latitude
761 measurement of snowfall (hilams) field campaign. *Bulletin of the American*
762 *Meteorological Society*, 103(8), E1762–E1780.
- 763 Cui, G., Bales, R., Rice, R., Anderson, M., Avanzi, F., Hartsough, P., & Conklin,
764 M. (2020). Detecting rain–snow–transition elevations in mountain basins using
765 wireless sensor networks. *Journal of Hydrometeorology*, 21(9), 2061–2081.
- 766 Dai, A. (2008). Temperature and pressure dependence of the rain-snow phase transi-
767 tion over land and ocean. *Geophysical Research Letters*, 35(12).
- 768 Ding, B., Yang, K., Qin, J., Wang, L., Chen, Y., & He, X. (2014). The dependence
769 of precipitation types on surface elevation and meteorological conditions and
770 its parameterization. *Journal of hydrology*, 513, 154–163.
- 771 Dolan, B., Rutledge, S. A., & Rasmussen, K. L. (2022). Multiscale interactions
772 contributing to enhanced orographic precipitation in landfalling frontal systems
773 over the olympic peninsula. *Monthly Weather Review*.
- 774 Field, P. R. (2000). Bimodal ice spectra in frontal clouds. *Quarterly Journal of the*
775 *Royal Meteorological Society*, 126(563), 379–392.
- 776 Fujiyoshi, Y., & Muramoto, K. (1996). The effect of breakup of melting snowflakes
777 on the resulting size distribution of raindrops. *Journal of the Meteorological*
778 *Society of Japan. Ser. II*, 74(3), 343–353.
- 779 Garcia-Benadi, A., Bech, J., Gonzalez, S., Udina, M., Codina, B., & Georgis, J.-F.
780 (2020). Precipitation type classification of micro rain radar data using an
781 improved doppler spectral processing methodology. *Remote Sensing*, 12(24),
782 4113.
- 783 Gatlin, P. N., Petersen, W. A., Knupp, K. R., & Carey, L. D. (2018). Observed re-
784 sponse of the raindrop size distribution to changes in the melting layer. *Atmo-*
785 *sphere*, 9(8), 319.
- 786 Gelaro, R., McCarty, W., Suárez, M. J., Todling, R., Molod, A., Takacs, L., ...
787 others (2017). The modern-era retrospective analysis for research and applica-
788 tions, version 2 (merra-2). *Journal of climate*, 30(14), 5419–5454.
- 789 Giangrande, S. E., Krause, J. M., & Ryzhkov, A. V. (2008). Automatic designation
790 of the melting layer with a polarimetric prototype of the wsr-88d radar. *Jour-*
791 *nal of Applied Meteorology and Climatology*, 47(5), 1354–1364.
- 792 Gorodetskaya, I. V., Tsukernik, M., Claes, K., Ralph, M. F., Neff, W. D., &
793 Van Lipzig, N. P. (2014). The role of atmospheric rivers in anomalous snow
794 accumulation in east antarctica. *Geophysical Research Letters*, 41(17), 6199–
795 6206.
- 796 Harpold, A. A., Kaplan, M. L., Klos, P. Z., Link, T., McNamara, J. P., Rajagopal,
797 S., ... Steele, C. M. (2017). Rain or snow: hydrologic processes, observations,
798 prediction, and research needs. *Hydrology and Earth System Sciences*, 21(1),
799 1–22.
- 800 Haynes, J. M., L’Ecuyer, T. S., Stephens, G. L., Miller, S. D., Mitrescu, C., Wood,
801 N. B., & Tanelli, S. (2009). Rainfall retrieval over the ocean with spaceborne
802 w-band radar. *Journal of Geophysical Research: Atmospheres*, 114(D8).
- 803 Helmus, J. J., & Collis, S. M. (2016). The python arm radar toolkit (py-art), a

- 804 library for working with weather radar data in the python programming lan-
 805 guage. *Journal of Open Research Software*, 4.
- 806 Henn, B., Weihs, R., Martin, A. C., Ralph, F. M., & Osborne, T. (2020). Skill
 807 of rain–snow level forecasts for landfalling atmospheric rivers: A multimodel
 808 assessment using californias network of vertically profiling radars. *Journal of*
 809 *Hydrometeorology*, 21(4), 751–771.
- 810 Hersbach, H., Bell, B., Berrisford, P., Hirahara, S., Horányi, A., Muñoz-Sabater, J.,
 811 ... others (2020). The era5 global reanalysis. *Quarterly Journal of the Royal*
 812 *Meteorological Society*, 146(730), 1999–2049.
- 813 Heymsfield, A. J., Bansemmer, A., Theis, A., & Schmitt, C. (2021). Survival of snow
 814 in the melting layer: Relative humidity influence. *Journal of the Atmospheric*
 815 *Sciences*, 78(6), 1823–1845.
- 816 Hirose, M., Shige, S., Kubota, T., Furuzawa, F. A., Minda, H., & Masunaga, H.
 817 (2021). Refinement of surface precipitation estimates for the dual-frequency
 818 precipitation radar on the gpm core observatory using near-nadir measure-
 819 ments. *Journal of the Meteorological Society of Japan. Ser. II*.
- 820 Hou, A. Y., Kakar, R. K., Neeck, S., Azarbarzin, A. A., Kummerow, C. D., Kojima,
 821 M., ... Iguchi, T. (2014). The global precipitation measurement mission.
 822 *Bulletin of the American Meteorological Society*, 95(5), 701–722.
- 823 Illingworth, A. J., Barker, H., Beljaars, A., Ceccaldi, M., Chepfer, H., Clerbaux, N.,
 824 ... others (2015). The earthcare satellite: The next step forward in global
 825 measurements of clouds, aerosols, precipitation, and radiation. *Bulletin of the*
 826 *American Meteorological Society*, 96(8), 1311–1332.
- 827 Jennings, K. S., Winchell, T. S., Livneh, B., & Molotch, N. P. (2018). Spatial vari-
 828 ation of the rain–snow temperature threshold across the northern hemisphere.
 829 *Nature communications*, 9(1), 1–9.
- 830 Klugmann, D., Heinsohn, K., & Kirtzel, H.-J. (1996). A low cost 24 ghz fm-cw
 831 doppler radar rain profiler. *Contributions to Atmospheric Physics/Beitraege*
 832 *zur Physik der Atmosphaere*, 61(9), 247–253.
- 833 Kneifel, S., Maahn, M., Peters, G., & Simmer, C. (2011). Observation of snowfall
 834 with a low-power fm-cw k-band radar (micro rain radar). *Meteorology and At-*
 835 *mospheric Physics*, 113(1), 75–87.
- 836 Knowles, N., Dettinger, M. D., & Cayan, D. R. (2006). Trends in snowfall versus
 837 rainfall in the western united states. *Journal of Climate*, 19(18), 4545–4559.
- 838 Kulie, M. S., Pettersen, C., Merrelli, A. J., Wagner, T. J., Wood, N. B., Dutter, M.,
 839 ... others (2021). Snowfall in the northern great lakes: lessons learned from
 840 a multisensor observatory. *Bulletin of the American Meteorological Society*,
 841 102(7), E1317–E1339.
- 842 Lamb, D., & Verlinde, J. (2011). Cold clouds. In *Physics and chemistry of clouds*
 843 (p. 457479). Cambridge University Press. doi: 10.1017/CBO9780511976377
 844 .013
- 845 Le, M., Chandrasekar, V., & Biswas, S. (2016). Evaluation and validation of gpm
 846 dual-frequency classification module after launch. *Journal of Atmospheric and*
 847 *Oceanic Technology*, 33(12), 2699–2716.
- 848 Lebsock, M. D., LEcuyer, T. S., Wood, N. B., Haynes, J. M., & Smalley, M. A.
 849 (2020). Status of the cloudsat mission. In *Satellite precipitation measurement*
 850 (pp. 25–43). Springer.
- 851 Lee, J.-E., Jung, S.-H., & Kwon, S. (2020). Characteristics of the bright band based
 852 on quasi-vertical profiles of polarimetric observations from an s-band weather
 853 radar network. *Remote Sensing*, 12(24), 4061.
- 854 Licznar, P., & Krajewski, W. F. (2016). Precipitation type specific radar reflectivity-
 855 rain rate relationships for warsaw, poland. *Acta Geophysica*, 64(5), 1840–
 856 1857.
- 857 Lin, D., Pickering, B., & Neely III, R. R. (2020). Relating the radar bright band
 858 and its strength to surface rainfall rate using an automated approach. *Journal*

- 859 of *Hydrometeorology*, 21(2), 335–353.
- 860 List, R., & Gillespie, J. (1976). Evolution of raindrop spectra with collision-induced
861 breakup. *Journal of Atmospheric Sciences*, 33(10), 2007–2013.
- 862 Liu, G. (2008). Deriving snow cloud characteristics from cloudsat observations.
863 *Journal of Geophysical Research: Atmospheres*, 113(D8).
- 864 Lundquist, J. D., Neiman, P. J., Martner, B., White, A. B., Gottas, D. J., & Ralph,
865 F. M. (2008). Rain versus snow in the sierra nevada, california: Comparing
866 doppler profiling radar and surface observations of melting level. *Journal of*
867 *Hydrometeorology*, 9(2), 194–211.
- 868 Maahn, M., Burgard, C., Crewell, S., Gorodetskaya, I. V., Kneifel, S., Lhermitte, S.,
869 ... van Lipzig, N. P. (2014). How does the spaceborne radar blind zone affect
870 derived surface snowfall statistics in polar regions? *Journal of Geophysical*
871 *Research: Atmospheres*, 119(24), 13–604.
- 872 Maahn, M., & Kollias, P. (2012). Improved micro rain radar snow measurements
873 using doppler spectra post-processing. *Atmospheric Measurement Techniques*,
874 5(11), 2661–2673.
- 875 Martner, B. E., Yuter, S. E., White, A. B., Matrosov, S. Y., Kingsmill, D. E., &
876 Ralph, F. M. (2008). Raindrop size distributions and rain characteristics in
877 california coastal rainfall for periods with and without a radar bright band.
878 *Journal of Hydrometeorology*, 9(3), 408–425.
- 879 Mateling, M. E., Pettersen, C., Kulie, M. S., Mattingly, K. S., Henderson, S. A., &
880 LEcuyer, T. S. (2021). The influence of atmospheric rivers on cold-season
881 precipitation in the upper great lakes region. *Journal of Geophysical Research:*
882 *Atmospheres*, 126(13), e2021JD034754.
- 883 Matrosov, S. Y. (2010). Cloudsat studies of stratiform precipitation systems ob-
884 served in the vicinity of the southern great plains atmospheric radiation
885 measurement site. *Journal of applied meteorology and climatology*, 49(8),
886 1756–1765.
- 887 Matrosov, S. Y., Cifelli, R., White, A., & Coleman, T. (2017). Snow-level esti-
888 mates using operational polarimetric weather radar measurements. *Journal of*
889 *Hydrometeorology*, 18(4), 1009–1019.
- 890 Matsuo, T., & Sasyo, Y. (1981). Melting of snowflakes below freezing level in the
891 atmosphere. *Journal of the Meteorological Society of Japan. Ser. II*, 59(1), 10–
892 25.
- 893 McIlhattan, E. A., Pettersen, C., Wood, N. B., & L’Ecuyer, T. S. (2020). Satellite
894 observations of snowfall regimes over the greenland ice sheet. *The Cryosphere*,
895 14(12), 4379–4404.
- 896 Meneghini, R., Iguchi, T., Seto, S., Yoshida, N., Awaka, J., & Kubota, T. (2021).
897 Gpm/dpr level 2 algorithm theoretical basis document (atbd).
- 898 Newman, A. J., Kucera, P. A., & Bliven, L. F. (2009). Presenting the snowflake
899 video imager (svi). *Journal of Atmospheric and Oceanic technology*, 26(2),
900 167–179.
- 901 Norin, L., Devasthale, A., L’Ecuyer, T., Wood, N., & Smalley, M. (2015). Inter-
902 comparison of snowfall estimates derived from the cloudsat cloud profiling
903 radar and the ground-based weather radar network over sweden. *Atmospheric*
904 *Measurement Techniques*, 8(12), 5009–5021.
- 905 Norin, L., Devasthale, A., & L’Ecuyer, T. S. (2017). The sensitivity of snowfall
906 to weather states over sweden. *Atmospheric Measurement Techniques*, 10(9),
907 3249–3263.
- 908 NWS. (2015). *Ncrfc zr display* (Vol. date of access = Dec 2021). NOAA’s National
909 Weather Service. Retrieved from [https://www.weather.gov/ncrfc/LMI_WOF](https://www.weather.gov/ncrfc/LMI_WOF_ZRDisplay)
910 _ZRDisplay
- 911 Pejčić, V., Saavedra Garfias, P., Mühlbauer, K., Trömel, S., & Simmer, C. (2020).
912 Comparison between precipitation estimates of ground-based weather radar
913 composites and gpm’s dpr rainfall product over germany.

- 914 Perry, L. B., Seimon, A., Andrade-Flores, M. F., Endries, J. L., Yuter, S. E., Ve-
 915 larde, F., ... others (2017). Characteristics of precipitating storms in glacier-
 916 ized tropical andean cordilleras of peru and bolivia. *Annals of the American*
 917 *Association of Geographers*, 107(2), 309–322.
- 918 Peters, G., Fischer, B., & Andersson, T. (2002). Rain observations with a vertically
 919 looking micro rain radar (mrr). *Boreal environment research*, 7(4), 353–362.
- 920 Pettersen, C., Bliven, L. F., Kulie, M. S., Wood, N. B., Shates, J. A., Anderson, J.,
 921 ... Wolff, D. B. (2021). The precipitation imaging package: Phase partitioning
 922 capabilities. *Remote Sensing*, 13(11), 2183.
- 923 Pettersen, C., Bliven, L. F., von Lerber, A., Wood, N. B., Kulie, M. S., Mateling,
 924 M. E., ... Wolff, D. B. (2020). The precipitation imaging package: Assessment
 925 of microphysical and bulk characteristics of snow. *Atmosphere*, 11(8), 785.
- 926 Pettersen, C., Kulie, M. S., Bliven, L. F., Merrelli, A. J., Petersen, W. A., Wagner,
 927 T. J., ... Wood, N. B. (2020). A composite analysis of snowfall modes from
 928 four winter seasons in marquette, michigan. *Journal of Applied Meteorology*
 929 *and Climatology*, 59(1), 103–124.
- 930 Petty, G. W. (2008). *A first course in atmospheric thermodynamics*. Sundog Pub-
 931 lishing.
- 932 Pfaff, T., Engelbrecht, A., & Seidel, J. (2014). Detection of the bright band with a
 933 vertically pointing k-band radar.
- 934 Prein, A. F., & Heymsfield, A. J. (2020). Increased melting level height impacts
 935 surface precipitation phase and intensity. *Nature Climate Change*, 10(8), 771–
 936 776.
- 937 Ryzhkov, A. V., & Zrnica, D. S. (2019). *Radar polarimetry for weather observations*
 938 (Vol. 486). Springer.
- 939 Sankaré, H., & Thériault, J. M. (2016). On the relationship between the snowflake
 940 type aloft and the surface precipitation types at temperatures near 0 c. *Atmo-*
 941 *spheric Research*, 180, 287–296.
- 942 Schauwecker, S., Rohrer, M., Huggel, C., Endries, J., Montoya, N., Neukom, R., ...
 943 Suarez, W. (2017). The freezing level in the tropical andes, peru: An indica-
 944 tor for present and future glacier extents. *Journal of Geophysical Research:*
 945 *Atmospheres*, 122(10), 5172–5189.
- 946 Schirle, C. E., Cooper, S. J., Wolff, M. A., Pettersen, C., Wood, N. B., L'Ecuyer,
 947 T. S., ... Nygård, K. (2019). Estimation of snowfall properties at a moun-
 948 tainous site in norway using combined radar and in situ microphysical observa-
 949 tions. *Journal of Applied Meteorology and Climatology*, 58(6), 1337–1352.
- 950 Screen, J. A., & Simmonds, I. (2012). Declining summer snowfall in the arctic:
 951 Causes, impacts and feedbacks. *Climate dynamics*, 38(11), 2243–2256.
- 952 Serio, M. A., Carollo, F. G., & Ferro, V. (2019). Raindrop size distribution and
 953 terminal velocity for rainfall erosivity studies. a review. *Journal of Hydrology*,
 954 576, 210–228.
- 955 Shates, J. A., Pettersen, C., L'Ecuyer, T., & Kulie, M. (2022). *Ground-Based Re-*
 956 *remote Sensing Observations at Marquette, Michigan*. Zenodo. Retrieved from
 957 <https://doi.org/10.5281/zenodo.7325232> doi: 10.5281/zenodo.7325232
- 958 Shates, J. A., Pettersen, C., L'Ecuyer, T. S., Cooper, S. J., Kulie, M. S., & Wood,
 959 N. B. (2021). High-latitude precipitation: Snowfall regimes at two distinct
 960 sites in scandinavia. *Journal of Applied Meteorology and Climatology*, 60(8),
 961 1127–1148.
- 962 Sims, E. M., & Liu, G. (2015). A parameterization of the probability of snow–rain
 963 transition. *Journal of hydrometeorology*, 16(4), 1466–1477.
- 964 Skofronick-Jackson, G., Hudak, D., Petersen, W., Nesbitt, S. W., Chandrasekar, V.,
 965 Durden, S., ... others (2015). Global precipitation measurement cold season
 966 precipitation experiment (gpex): for measurements sake, let it snow. *Bulletin*
 967 *of the American Meteorological Society*, 96(10), 1719–1741.
- 968 Skofronick-Jackson, G., Kulie, M., Milani, L., Munchak, S. J., Wood, N. B., & Lev-

- 969 izzani, V. (2019). Satellite estimation of falling snow: A global precipitation
 970 measurement (gpm) core observatory perspective. *Journal of applied meteorol-*
 971 *ogy and climatology*, 58(7), 1429–1448.
- 972 Skofronick-Jackson, G., Petersen, W. A., Berg, W., Kidd, C., Stocker, E. F.,
 973 Kirschbaum, D. B., . . . others (2017). The global precipitation measurement
 974 (gpm) mission for science and society. *Bulletin of the American Meteorological*
 975 *Society*, 98(8), 1679–1695.
- 976 Slinskey, E. A., Loikith, P. C., Waliser, D. E., Guan, B., & Martin, A. (2020). A
 977 climatology of atmospheric rivers and associated precipitation for the seven
 978 us national climate assessment regions. *Journal of Hydrometeorology*, 21(11),
 979 2439–2456.
- 980 Steiner, M., Smith, J. A., & Uijlenhoet, R. (2004). A microphysical interpretation of
 981 radar reflectivity–rain rate relationships. *Journal of the atmospheric sciences*,
 982 61(10), 1114–1131.
- 983 Stephens, G. L., Vane, D. G., Tanelli, S., Im, E., Durden, S., Rokey, M., . . . others
 984 (2008). Cloudsat mission: Performance and early science after the first year of
 985 operation. *Journal of Geophysical Research: Atmospheres*, 113(D8).
- 986 Stewart, R. E., Thériault, J. M., & Henson, W. (2015). On the characteristics of and
 987 processes producing winter precipitation types near 0 c. *Bulletin of the Ameri-*
 988 *can Meteorological Society*, 96(4), 623–639.
- 989 Tamang, S. K., Ebtehaj, A. M., Prein, A. F., & Heymsfield, A. J. (2020). Link-
 990 ing global changes of snowfall and wet-bulb temperature. *Journal of Climate*,
 991 33(1), 39–59.
- 992 Tobin, D. M., Kumjian, M. R., & Black, A. W. (2021). Effects of precipitation
 993 type on crash relative risk estimates in kansas. *Accident Analysis & Preven-*
 994 *tion*, 151, 105946.
- 995 Uplinger, W. (1981). A new formula for raindrop terminal velocity. In *Conference on*
 996 *radar meteorology, 20 th, boston, ma* (pp. 389–391).
- 997 Valdivia, J. M., Gatlin, P. N., Kumar, S., Scipión, D., Silva, Y., & Petersen, W. A.
 998 (2022). The gpm-dpr blind zone effect on satellite-based radar estimation of
 999 precipitation over the andes from a ground-based ka-band profiler perspective.
 1000 *Journal of Applied Meteorology and Climatology*, 61(4), 441–456.
- 1001 von Lerber, A., Moisseev, D., Leinonen, J., Koistinen, J., & Hallikainen, M. T.
 1002 (2014). Modeling radar attenuation by a low melting layer with optimized
 1003 model parameters at c-band. *IEEE Transactions on Geoscience and Remote*
 1004 *Sensing*, 53(2), 724–737.
- 1005 Wang, P., & Pruppacher, H. (1977). Acceleration to terminal velocity of cloud and
 1006 raindrops. *Journal of Applied Meteorology (1962-1982)*, 275–280.
- 1007 Watters, D., Battaglia, A., Mroz, K., & Tridon, F. (2018). Validation of the gpm
 1008 version-5 surface rainfall products over great britain and ireland. *Journal of*
 1009 *Hydrometeorology*, 19(10), 1617–1636.
- 1010 White, A. B., Gottas, D. J., Strem, E. T., Ralph, F. M., & Neiman, P. J. (2002). An
 1011 automated brightband height detection algorithm for use with doppler radar
 1012 spectral moments. *Journal of Atmospheric and Oceanic Technology*, 19(5),
 1013 687–697.
- 1014 Williams, C. R., Ecklund, W. L., & Gage, K. S. (1995). Classification of precipitat-
 1015 ing clouds in the tropics using 915-mhz wind profilers. *Journal of Atmospheric*
 1016 *and Oceanic Technology*, 12(5), 996–1012.
- 1017 You, Y., Peters-Lidard, C., Ringerud, S., & Haynes, J. M. (2021). Evaluation of
 1018 rainfall-snowfall separation performance in remote sensing datasets. *Geophys-*
 1019 *ical Research Letters*, 48(21), e2021GL094180.
- 1020 Yuter, S. E., Kingsmill, D. E., Nance, L. B., & Löffler-Mang, M. (2006). Obser-
 1021 vations of precipitation size and fall speed characteristics within coexisting
 1022 rain and wet snow. *Journal of Applied Meteorology and Climatology*, 45(10),
 1023 1450–1464.